Recent advances on additive manufactured shape memory alloys

Yu-xi YANG[1], Wei-hong GAO[1], Bin SUN[1], Yu-dong FU[1], Xiang-long MENG[2]

1. College of Materials Science and Chemical Engineering, Harbin Engineering University, Harbin 150001, China;
2. School of Materials Science and Engineering, Harbin Institute of Technology, Harbin 150001, China

Abstract: Additive manufacturing (AM), as a revolutionary technology, enables the fabrication of complex shape memory alloy (SMA) components with unprecedented degrees of freedom, thus providing tremendous opportunities for developing modern manufacturing and transforming traditional manufacturing. Herein, this review aims to broaden ideas for preparing AM-built SMAs with high performance and multifunctionality through elucidating of the current advancements from the perspectives of the microstructure, properties, and prospects. It is concluded that the columnar grains formed by epitaxial solidification, and the prominent microstructure characteristics during printing, are modulated by different scanning parameters. The combined effects of microstructures, such as precipitates, dislocations, twins and stacking faults, can lead to desirable materials with excellent and stable shape memory effect and superelastic effect. Finally, further breakthroughs in materials, technologies, properties and methods are needed to facilitate applicability in various industries.

Key words: shape memory alloy; additive manufacturing; epitaxial solidification; martensite transformation; process parameter control

1 Introduction

Additive manufacturing (AM), also regarded as 3D printing, is a technology that achieves metallurgical bonding through layer-by-layer construction based on a computer-designed 3D model [1−3]. AM presents distinct advantages of low feedstock wastage, fast molding speed, and various designing shapes, not achievable conventionally. Therefore, this advanced and intelligent approach has great potential to satisfy the demand for efficient customizability. Shape memory alloys (SMAs) have highly provoked attention in AM field, because this process enables SMAs to retain the typical shape memory effect (SME) or superelasticity effect (SE) [4,5]. To date, AM technology has been used to successfully fabricate NiTi-based SMAs (NiTi-SMAs) [6−8], copper-based SMAs (Cu-SMAs) [9], iron-based SMAs (Fe-SMAs) [10] and others, as shown in Fig. 1. AM-fabricated SMAs have significant value and broad application prospects in the domains of aerospace, automotive manufacturing, robotics, biomedicine, civil engineering, and so on [15−17]. However, the presence of impurity elements in the raw material and the tendency of elemental burnout during the AM implementations possibly result in inhomogeneous composition and metallurgical defects [18]. Therefore, the exploitation of AM-built SMAs with desirable microstructure, high performance, and multifunctionality is a formidable challenge. Nowadays, relative research has sprung up explosively, which provides the experimental basis for adjusting the microstructure and properties of AM-processed SMAs.
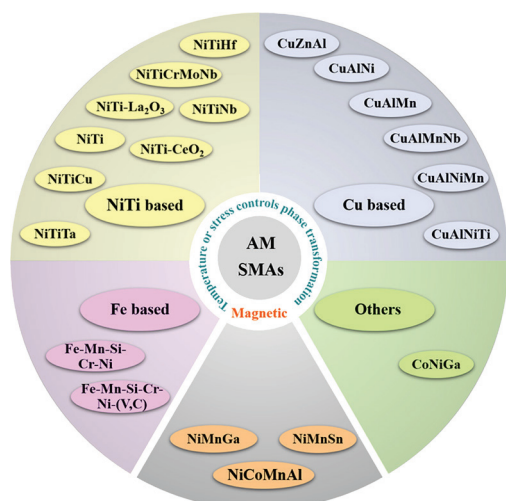
Corresponding author: Wei-hong GAO, Tel: +86-18045625109, E-mail: gaoweihong@hrbeu.edu.cn;
Yu-dong FU, Tel: +86-15204692272, E-mail: fuyudong@hrbeu.edu.cn

Fig. 1 Types of SMAs through AM (Magnetic shape memory alloys and others are mentioned in Refs. [11−14])

It should be noted that more and more review papers concentrating on AM-fabricated SMAs have been published. Especially, PARVIZI et al [19] discussed the effects of critical steps in AM process on the microstructures and properties of NiTi-SMAs, including powder preparation, laser parameters, and fabrication chamber. Besides NiTi SMAs, ALAGHA et al [20] also investigated Cu-SMAs and NiMnGa-SMAs achieved by powder bed fusion (PBF). These studies have provided important information on the microstructures and properties of AM-produced SMAs. However, a review with a detailed subset of the microstructures and properties is still lacking. Therefore, due to the upgrading of technology, the expansion of SMA types, and the application of heat treatment processes, a timely summary of insightful works can provide guidance for tuning and optimizing microstructures and properties. This review will present details of the microstructures, properties, and perspectives of SMAs by AM. Herein, we start with characteristics of AM applied in SMAs systems, followed by standard AM technologies. Thereafter, the microstructure characterization of AM-fabricated SMAs will be presented from the perspectives of the defect and relative density, melt pool and grain structure, precipitation, dislocation, twin and stacking fault, and phase transformation behavior. Moreover, we will discuss the properties of AM-built SMAs, including tensile and compressive properties, SME, SE, and elastocaloric effect. Last, the perspectives will be illustrated,

especially the research direction and the application prospect.

2 Additive manufacturing of SMA

Currently, AM-produced SMAs are usually attained by the following three approaches: powder bed fusion (PBF), direct energy deposition (DED), and binder jet (BJ) [21−23]. PBF includes selective laser melting (SLM), electron beam melting (EBM), etc. The specific process procedures of PBF are (1) laying powder in the powder bed by a roller mechanism; (2) melting the powder through a heat source to build a deposition layer; (3) repeating the operation until the manufacture is completed [24]. DED involves more printing technologies, such as laser-engineered net shaping (LENS), laser-based directed energy deposition (LDED), electron beam free forming fabrication (EBF³), wire arc additive manufacturing (WAAM), etc [25,26]. In the DED process, the raw material (powder or wire) is delivered through the nozzle or wire feeder. Thereby, DED exhibits more advantages by comparison to PBF: (1) higher deposition rates, for instance, 0.5 kg/h for LENS [27] and up to 10 kg/h for WAAM [28]; (2) capable of preparing composition gradient materials with multiple feeders; (3) superior in constructing large-scale components; (4) filling cracks or modifying parts. However, the high surface roughness of the DED-built parts causes the requirement for further machining. Furthermore, due to different heat sources, AM technology can be classified as laser AM, electron beam AM, and plasma arc AM. Their cooling rates are 10^5-10^7 K/s (SLM) [29], 10^3-10^5 K/s (EBM) [30] and 10^2-10^3 K/s (WAAM) [31], respectively. Among them, electron beam performs higher power and energy per volume, contributing to greater productivity. Distinctly different from PBF and DED with the heat source, BJ employs binder materials to attach the powder. This method does not involve the heat source, which circumvents the issues induced by excess heating. Besides, it has emerged as cost-effective technology (the heat source with complex structure is expensive) [32]. However, due to the large porosity of the parts, further processing is necessary to improve the microstructure and increase strength. In general, the main representative categories for AM techniques are SLM, EBM, LDED, and WAAM, which are demonstrated in Fig. 2.
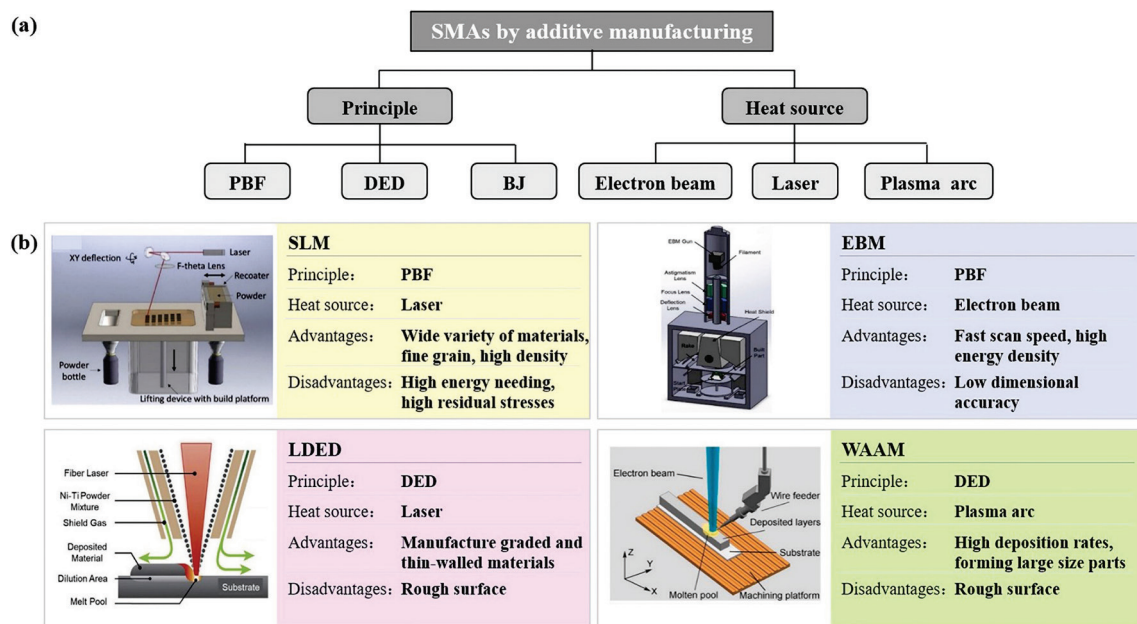
Fig. 2 AM methods for manufacturing SMAs: (a) AM classification by principles and different heat sources; (b) Characteristics of AM [33,34] (Copyright 2019, Elsevier; Copyright 2021, Elsevier)

In the field of AM, appropriate combination of parameters contributes to enhancing the structural integrity and performance of SMAs. Various parameters involve wire feed rate, powder feed rate, laser power (P), scanning velocity (V), hatching space (H), layer thickness (T), energy density (E), scanning strategy, etc [35−37]. Among them, E is calculated by $E=P/(VHT)$ [38]. These relevant parameters, which are the focus of discussion in this work, are the most concerning in the literature, as illustrated in Table 1 and Table 2. Another important factor is the nature of the raw material, including the impurity content [88], powder particle size [33], and powder composition [58]. Additionally, there are also other implications, such as the pressure of protective gas [89].

3 Microstructure characterization of SMAs by additive manufacture

The complex thermal behavior of AM results in SMAs with spatially variable microstructures. Exploring the evolution of microstructure can contribute to improving the performance and promoting the applications.

3.1 Defect and relative density

During the AM process, defects in the components will induce crack expansion, which deteriorates the mechanical properties. Generally, optimizing and controlling process parameters can reduce defects to obtain samples with high relative density.

In multi-scale and multi-physical field coupled additive manufacturing processes, SMAs suffer from defects, for instance, lack of fusion defects, keyholes, balling defects, and cracks. The following studies reveal the causes of defect formation in NiTi-SMAs. XUE et al [90] compared the single track of $Ni_{50.8}Ti_{49.2}$ alloy with different P and V in the LPBF method, as shown in Fig. 3. When the linear energy density was high, there were keyholes induced by the metal vapor in the deep melt pool. Since the escape rate of gas from the melt pool is less than the solidification rate, the gas is wrapped by the solidified structure, thus forming keyholes. By contrast, the tracks exhibited discontinuous gaps and were not fused to the substrate, when the linear energy density was low. The laser or electron beam energy shows the Gaussian distribution, and there is a certain overlap area in the melting area. If the depth of the overlap zone is less than the thickness of the powder layer, there is unmelted powder, resulting in the lack of fusion defects. Besides, balling defects (tracks of discontinuity but fused with the substrate) occurred when both P and V were high. Overall, the uniform track with a depth greater than thickness was defined as the optimal

Table 1 Detailed SMAs used for AM

SMA	AM	P/W	V	H/μm	T/μm	Ref.
$Ni_{50}Ti_{50}$ (wt.%)	SLM	150	200−1000 mm/s	100	50	[33]
$Ni_{50.2}Ti_{49.8}$ (at.%)	SLM	50−70	75−150 mm/s			[39]
$Ni_{50.4}Ti$ (at.%)	SLM	150−250	600−1100 mm/s	120	30	[40]
$Ni_{49.4}Ti_{50.6}$ (at.%)	SLM	70	80−150 mm/s	100	30	[41]
$Ni_{55.8}Ti$ (wt.%)	SLM	75−200	400−1200 mm/s	80−120	20−40	[42]
$Ni_{50.4}Ti_{49.6}$	SLM	70	120 mm/s	100	30	[43]
$Ni_{50}Ti_{50}$ (at.%)	SLM	200	500−2000 mm/s	100	50	[44]
$Ni_{51.4}Ti$ (at.%)	SLM	200	1500 mm/s	40−80	40	[45]
$Ni_{50.8}Ti_{49.2}$ (at.%)	SLM	250	1.25 m/s	120	30	[46]
$Ni_{50}Ti_{50}$ (at.%)	SLM	100−200	5−40 m/min	80	40	[47]
$Ni_{55.98}Ti$ (wt.%)	SLM	60−200	40−1200 mm/s	40−110	30	[48]
$Ni_{55}Ti_{45}$ (wt.%)	SLM	75−250	225−1500 mm/s	120	50	[49]
$Ni_{49.4}Ti_{50.6}$ (at.%)	SLM	70	105 mm/s	100	30	[50]
$Ni_{50.4}Ti$ (at.%)	SLM	120	500 mm/s	80	30	[51]
$Ni_{50.6}Ti_{49.4}$	SLM	250	1200 mm/s	60	50	[52]
$Ni_{55.4}Ti$ (wt.%)	SLM	40	160 mm/s	120	30	[53]
$Ni_{55.4}Ti$ (wt.%)	SLM	250	1100 mm/s	120	30	[53]
$Ni_{50.8}Ti$ (at.%)	SLM	250	1250 mm/s	80		[54]
$Ni_{49.9}Ti$ (at.%)	SLM	120−180	600−1200 mm/s	40−70	40	[55]
$Ni_{50.73}Ti$ (at.%)	SLM	180	1000 mm/s	120	30	[56]
$Ni_{50.6}Ti_{49.4}$ (wt.%)	SLM	200−375	1000−1400 mm/s	60	30	[57]
$Ni_{50.6}Ti_{49.4}$ (at.%)	SLM	70	105 mm/s	100	30	[58]
$Ni_{50.8}Ti_{49.2}$ (at.%)	LSF	1500−1800	480−720 mm/min	600	150	[59]
$Ni_{50.8}Ti_{49.2}$	LSF	1500	600 mm/min	600	150	[60]
$Ni_{50.4}Ti_{29.6}Hf_{20}$ (at.%)	LPBF	100−250	200−1000 mm/s	60−140	30	[61]
$NiTi−CeO_2$	LPBF	125	600 mm/s	80	30	[62]
$CuAl_{11.85}Mn_{3.99}Nb_{1.64}$ (wt.%)	SLM	200−250	500−600 mm/s	90	30	[63]
$Cu_{71.6}Al_{17}Mn_{11.4}$ (at.%)	SLM	200−350	500−2000 mm/s	90−150		[9]
CuZnAl	SLM	200−350	300−700 mm/s	90	40	[64]
$Cu_{81.95}Al_{11.85}Ni_{3.2}Mn_3$ (wt.%)	SLM	230−280	200−600 mm/s			[65]
$CuAl_{13.5}Ni_4Ti_{0.5}$	SLM	250−340	600−900 mm/s	90	40	[66]
$CuAl_{11.85}Ni_{3.2}Mn_3$	SLM	330	740 mm/s		90	[67]
$CuAl_{11.35}Ni_{3.2}Mn_3Zr_{0.5}$	SLM	330	740 mm/s		80	[67]
$FeMn_{17}Si_5Cr_{10}Ni_4$ (wt.%)	LPBF	420	800 mm/s	100	50	[68]
$FeMn_{17}Si_5Cr_{10}Ni_4$ (wt.%)	LPBF	380−420	800 m/s	100	50	[69]
$FeMn_{17}Si_5Cr_{10}Ni_4$ (wt%)	LPBF	115−175	300−600 mm/s	100	30	[70]
$FeMn_{17}Si_5Cr_{10}Ni_4 (V,C)_1$ (wt.%)	LPBF	175	100−400 mm/s	100	30	[10]

SLM−Selective laser melting; LPBF−Laser-based powder bed fusion; LSF−Laser solid forming; P−Laser power, V−Scanning velocity, H−Hatching space, T−Layer thickness

Table 2 Detailed SMAs used for AM with different feeding rates

SMA	AM	Feeding rate	Ref.
$Ni_{55}Ti_{45}$ (at.%)	DED	3.5 g/min	[71]
$Ni_{50.93}Ti_{49.07}$ (at.%)	DED	0.015 g/s	[72]
$Ni_{50.93}Ti_{49.07}$ (at.%)	DED	0.96 g/min	[73]
$Ni_{50}Ti_{50}$ (wt.%)	DED	5 g/min	[33]
$Ni_{56}Ti$ (wt.%)	LENS	5 g/min	[74]
$Ni_{58}Ti_{42}$ (wt.%)	LDED	12 g/min	[75]
$Ni_{55.78}Ti$ (wt.%)	EBF³	3 m/min	[76]
$Ni_{50.7}Ti$ (at.%)	EBF³	3 m/min	[77]
$Ni_{50.7}Ti$ (at.%)	EBF³	2.5−3 m/min	[78]
$Ni_{50.8}Ti_{49.2}$	WAAM	1500 mm/min (Ti), 1045 mm/min (Ni)	[79]
$Ni_{53}Ti_{47}$	WAAM	1500 mm/min (Ti), 1146 mm/min (Ni)	[79]
$Ni_{55.74}Ti$ (wt.%)	WAAM	4−8 m/min	[80]
$Ni_{52}Ti$ (at.%)	WAAM	700 mm/min (Ti), 513 mm/min (Ni)	[81]
$Ni_{50.5}Ti$ (at.%)	WAAM	0.9 m/min	[82]
$Ni_{50.9}Ti_{49.1}$	WAAM	4.3 m/min	[83]
$Ni_{50.8}Ti$ (at.%)	WAAM	7.4−8.9 m/min	[84]
TiNiCu	LAM	3−8 g/min	[85]
TiNiCu	LAM	5−8 g/min	[86]
NiTiTa	WAAM	800 mm/min	[8]
Ni–Ti–Cr–Mo–Nb	WAAM	1000 mm/min	[7]
$NiTi−La_2O_3$	LAM	8 g/min	[87]

DED−Direct energy deposition; LENS−Laser engineered net shaping; LDED−Laser-based directed energy deposition; EBF³− Electron beam free forming fabrication; WAAM−Wire arc additive manufacturing
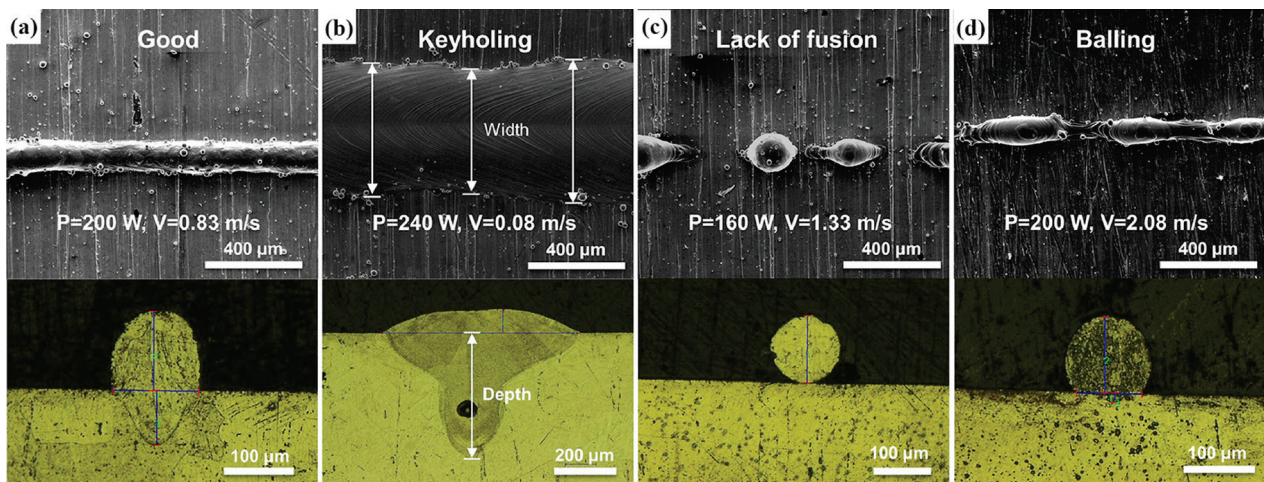
Fig. 3 Morphology of single-tracks fabricated by LPBF: (a) Good quality; (b) Keyholing; (c) Lack of fusion; (d) Balling defects [90] (Copyright 2021, Elsevier)

track. Moreover, CHEKOTU et al [55] observed cracks on the surface of $Ni_{49.9}Ti_{50.1}$ SMAs (V= 1200 mm/s, P=150 W, H=40 μm). The increased crack susceptibility is attributed to the steeper temperature gradients produced by multiple melting and solidification [51]. Furthermore, other sorts of SMAs also exhibit similar defects which may be sensitive to scanning parameters, for example, NiTiHf SMAs [91], Cu-SMAs [65], and Fe-SMAs [70].

The formation of defects is associated with process procedures; therefore, higher density will be gained by selecting more appropriate parameters. Within a certain range, increasing P or decreasing V can obtain high relative density. For example, LU et al [39] employed SLM to print $Ni_{50.2}Ti_{49.8}$ SMAs and noticed this phenomenon in the range of 50−70 W and 75−150 mm/s, as shown in Fig. 4. Similarly, it also applies to Cu-SMAs (240− 340 W and 600−700 mm/s) [66] and Fe-SMAs (115−175 W and 300−600 mm/s) [70]. In this regard, the correlation between H and relative density is less well studied. WANG et al [48] concluded that the relative density of NiTi SMAs was more incredible than 98.9%, as H rose from 40 to 70 μm. For most SMAs (NiTi-SMAs, Cu-SMAs, Fe-SMAs), nearly fully-dense components have been successfully produced. For NiTi SMAs, XUE et al [90] thought that E in the range from 50 to 200 J/mm³ was capable of printing NiTi SMAs with higher relative densities. Concerning Cu-SMAs, the relative density of CuZnAl SMAs grew, and then dropped with E (50 to 350 J/mm³) [64]. When E

was 277.8 J/mm³, the relative density reached its maximum. For Fe-SMAs, FERRETTO et al [70] introduced that the relative density of Fe− 17Mn−5Si−10Cr−4Ni SMAs prepared by LPBF increased as E rose. When the laser power was maximum (175 W) and the scanning speed was minimum (300 mm/s), a high density of 99.8% was also obtained. Therefore, each parameter in the work should be set and validated to develop other SMAs with high relative density. An Eagar Tsai (E-T) model for predicting melt pool geometry and defect type has been recently proposed. XUE et al [90] selected suitable machining parameters and produced a near defect-free cube based on the process parameter diagrams of $Ni_{50.8}Ti_{49.2}$ and $Ni_{50.1}Ti_{49.9}$, as shown in Fig. 5.

In summary, the melting and solidification behavior, the characteristics of tracks, and the continuity between the layers depend on process parameters. To achieve high-density SMAs, prediction by modeling is required prior to actual printing. Subsequently, the optimization of the processing parameters plays a prominent role in defect prevention.

3.2 Melt pool and grain structure

In contrast to the conventional processing techniques, AM-prepared SMAs undergo a dynamic cyclic heating and cooling process, which complicates the melt pool and grain structure.

The melting and solidification of the melt pool affect the structural characteristics of the grains, so comprehending the geometry of the melt pool helps
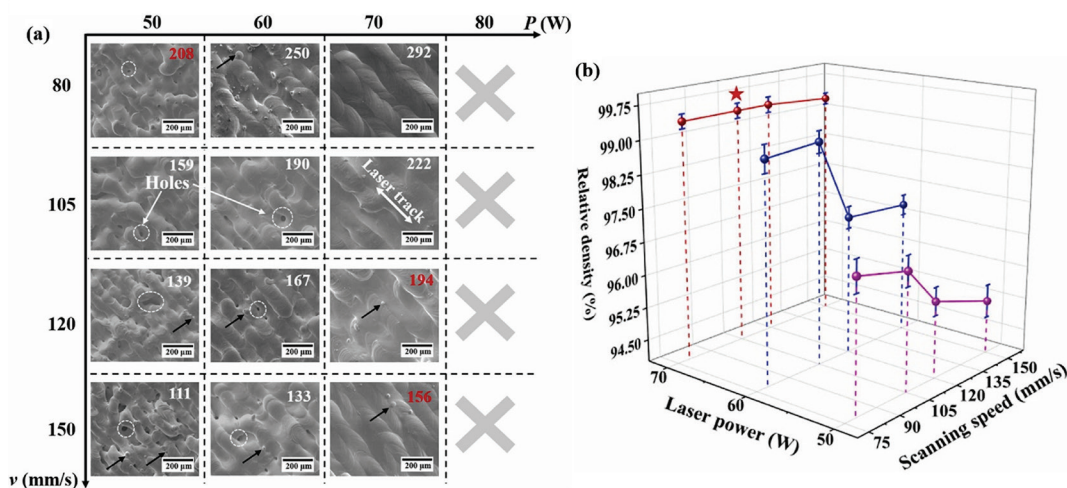
Fig. 4 Research results of $Ni_{50.2}Ti_{49.8}$ alloys printed by SLM with different V and P: (a) SEM images; (b) Variation of relative density with V and P [39] (Copyright 2022, Elsevier)
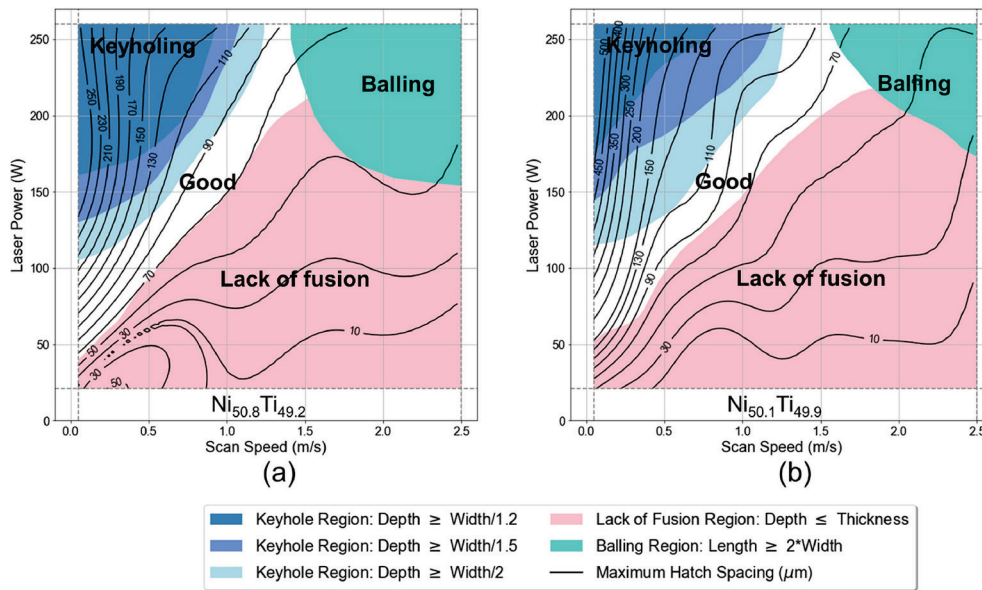
Fig. 5 Process parameter maps of Ni$_{50.8}$Ti$_{49.2}$ (a) and Ni$_{50.1}$Ti$_{49.9}$ (b) with E-T model [90] (Copyright 2021, Elsevier)

to build SMAs with the desired microstructure. The heat dissipation downward provides the melt pool with a curved elliptical shape, and its dimensions are related to the deposited layer thickness and scanning parameters. The depth of the melt pool is generally observed along the building direction, while the width of that is measured perpendicular to the building direction. By observing the melt pool of Ni$_{49.7}$Ti$_{50.3}$ SMAs, FARHANG et al [92] noticed that the average depth of the melt pool increased from 31 to 46 μm as the deposited layer thickness increased. In addition, the melt-pool width from the surface to the central part significantly declined (from 115 to 79 μm) along the horizontal direction. The main reasons for these phenomena are: (1) The metal in the top area after printing is more uniformly heated than the bottom area (a characteristic of laser scanning), so the melt pool is deeper. (2) The metal near the surface exhibits a higher cooling rate; therefore, it can shorten the penetration time in the vertical direction, resulting in a wider melt pool. Furthermore, the melt-pool scale highly depends on the scanning parameters. The larger the P or the smaller the V, the deeper and wider the melt pool is [41]. This phenomenon is also available for Fe-SMAs [10]. This is because the ascent in V leads to a sharp fall in energy and rapid heat dissipation. Interestingly, the melt-pool depth of NiTi SMAs increased consistently from 220 to 330 μm with the simultaneous growth of P

and V (with constant E). E, as a thermodynamically relevant parameter, is unable to reflect flow-related physical phenomena, such as the typical Marangoni flow [93]. Therefore, whether E is a factor impacting the melt-pool depth is further examined. When exploring the melt pool situation, the stability of the flow occurring during deposition and the heat transfer between liquid and solid (conduction, surface radiation, etc) need to be concentrated on.

Epitaxial solidification is widely observed in AM-fabricated SMAs along the building direction, manifested by the generation of columnar grains. Under certain solidification conditions, equiaxed grains appear at the termination of the columnar grain growth. The main reason for this micro-structural change is the alteration in subcooling degree ΔT, the temperature gradient G, and the solidification rate R for different regions of the alloy during solidification. It is worth mentioning that G/R determines the grain morphology; therefore, the transition from columnar to equiaxed grains emerges as the ratio descends. RESNINA et al [83] pointed out that the intermediate region has a high-temperature gradient, which induces the growth of columnar grains in the gradient direction. This typical epitaxial solidification phenomenon also occurred in other SMAs, such as NiTi-SMAs [82,94], Cu-SMAs [95,96], and Fe-SMAs [69,70]. Moreover, it has been shown that other grain characteristics are significantly related

to the variation of E. Generally, the higher E means adequate energy and time for nucleation and growth. GAN et al [40] detected that the average grain size of NiTi-SMAs (equiaxed grains) rose substantially from (570±23) to (1570±67) nm as E climbed (37.88−99.21 J/mm^3). However, unlike NiTi-SMAs or Cu-SMAs, Fe-SMAs are extremely special during the solidification. FERRETTO et al [70] found that when E increased from 63.89 to 194.44 J/mm^3, Fe−17Mn−5Si−10Cr−4Ni SMAs changed from columnar crystals (average grain size of about 60 µm) to equiaxed crystals (diameter less than 10 µm), as demonstrated in Fig. 6. This work also verified that non-uniform nucleation of the γ phase occurs at the grain boundary of δ phase in the high E case.

The microstructure is correlated with the scanning strategy and parameters when analyzing from the perspective perpendicular to the building direction. The scanning strategy defines the scanning paths within and between neighboring layers. For constructing SMAs, common modes include intra-layer unidirectional, intra-layer nip

angle of 90°, and inter-layer nip angle of 90°, among others. FU et al [97] utilized different angles between neighboring tracks to print Ni$_{55.5}$Ti$_{44.5}$ SMAs. They described that when the scanning angle was 45°, the grains formed a herringbone pattern, which was attributed to the formation of the heat flow along the transverse direction. When the scanning angles were 60° and 90°, irregular tracks were generated during the printing process, implying an unstable melt pool. Furthermore, S-shaped grains and square-shaped grains can be noticed at an angle of 90° [45,46]. EHSAN SAGHAIAN et al [98] explored that the size of square grains was associated with H, as presented in Fig. 7. It was shown that an ascend in H declined the number of tracks. Also, it allowed the previous layer to cool with enough time, decreasing the melting parts of the previously solidified layer. Because of the formation of the solidification front with columnar morphology through selecting the appropriate parameters (P=250 W, C=1250 mm/s, H=120 µm), the perfect square-shaped grains were produced.
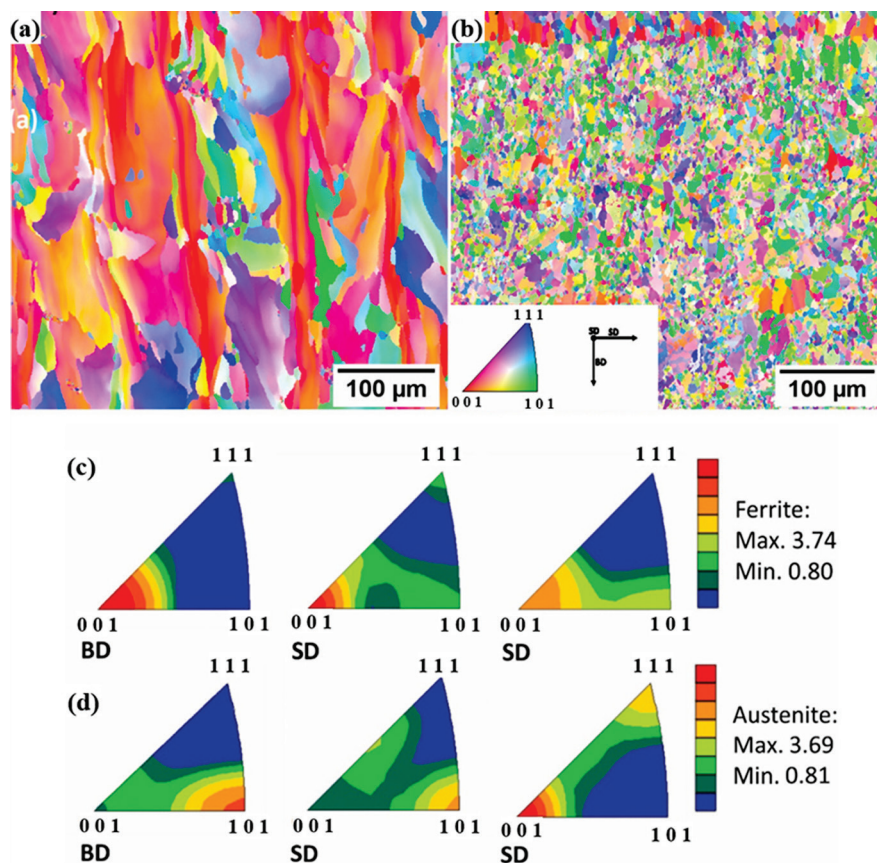
Fig. 6 EBSD analysis result of Fe−Mn−Si−Ni−(V,C) by LPBF: (a, c) Low E, (b, d) High E [70] (Copyright 2021, Elsevier)
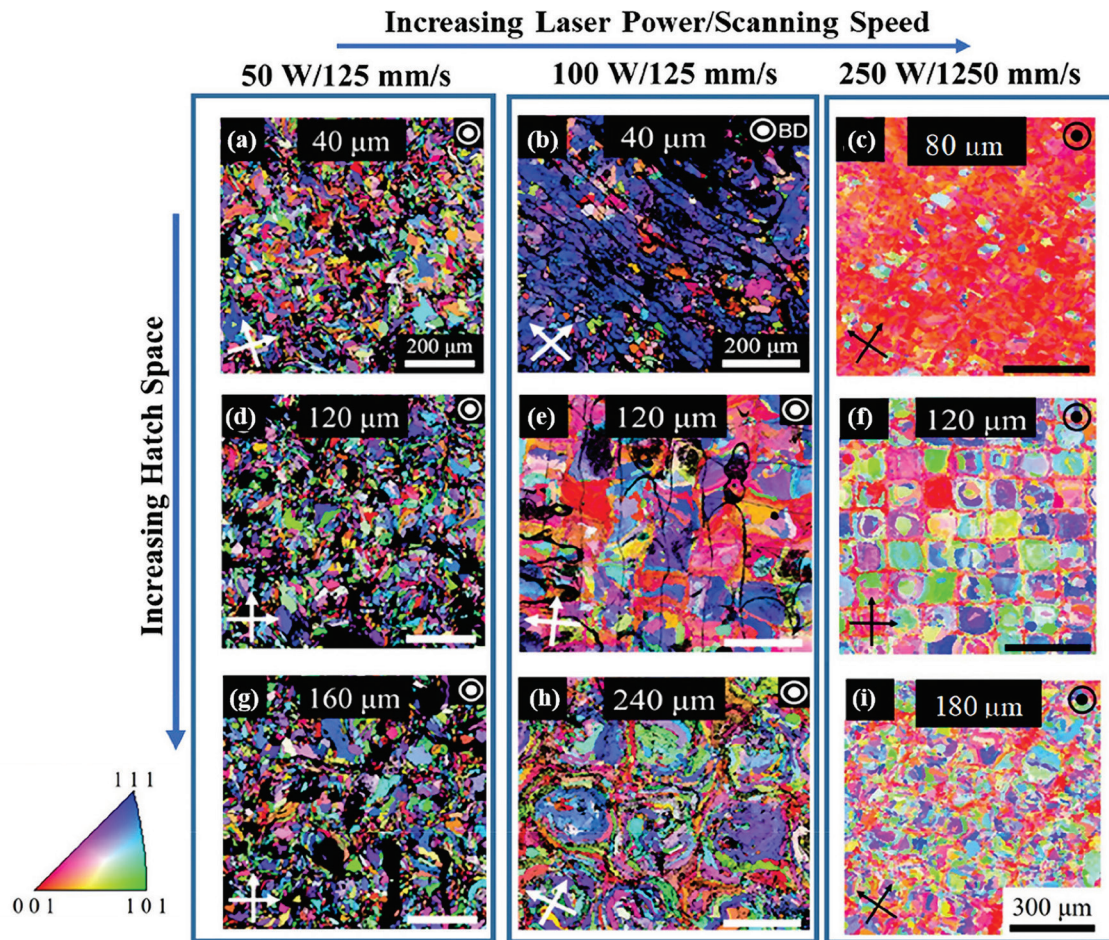
Fig. 7 IPF maps for NiTi SMAs fabricated by LPBF with *H* [98] (Copyright 2022, Elsevier)

Although no mechanical processing was involved in the AM process, the grains of SMAs exhibited a distinct [001] orientation. The columnar grains (along the BD direction) in NiTi SMAs developed into cube texture {001}⟨100⟩ and Goss texture {110}⟨001⟩. The crystallographic orientation of equiaxed grains along the horizontal direction belonged to {001}⟨100⟩ cube texture [76]. AM-printed Cu-SMAs [9] and Fe-SMAs [10] were also identified to possess the [001] texture. The solidification texture derives from the preferential growth of grains along the direction of the maximum thermal gradient [54,81], so the texture strength is related to the direction of heat flow. In general, the bottom region at the beginning of solidification has a faster cooling rate, and heat dissipation to the solidified part occurs not strictly parallel to the building direction. Consequently, PU et al [34] presented the gradual enhancement of the [001] texture with increased deposition-layer height in NiTi SMA built by WAAM. Because the changes in process parameters during printing determine the degree of remelting of the solidified layer, they are considered factors affecting the texture strength. For example, REN et al [99] showed that higher *P* and *V* enhanced the temperature gradient and promoted the continuous growth of columnar grains, thus enhancing the ⟨100⟩//BD texture in NiTi SMAs. However, another result highlighted that the grain orientation was modified by altering *E* in Fe-SMAs. Specifically, *E* promoted the phase transformation, which caused the development from ⟨001⟩ texture to ⟨101⟩ one for austenite grains [10,70].

In summary, during the AM process, the microstructure depends on the melt pool characteristics, and the evolution of grain structure impacts the texture structure. By governing the scanning parameters and processing strategies, the melt pool and grains can be effectively regulated.

3.3 Precipitation, dislocation, twin and stacking fault

The interaction of precipitations, dislocations, twins, and stacking faults in AM-produced SMAs

are pivotal in the martensite transformation, thus affecting properties such as strength, SME and SE.

According to different SMA components, there are multiple types of precipitates. Irrespective of the kind of precipitations, thermodynamic and kinetic conditions for nucleation and growth entail being satisfied. Recent studies have been focused on precipitates in NiTi-SMAs, including titanium-rich precipitates, Ti_2Ni and $Ti_4Ni_2O_x$, nickel-rich precipitates, Ni_4Ti_3 and Ni_3Ti, and so on. The morphology, the orientation relationship, and the causes of precipitation have received more attention. The appearance of Ti_2Ni precipitates is widely reported [100,101]. FENG et al [59] employed LSF to fabricate $Ni_{50.8}Ti_{49.2}$ and dedicated that long strips of Ti_2Ni precipitates existed. Specifically, the lower boiling point of Ni (3186 K) than Ti (3560 K) results in the evaporation of Ni from the melt pool. Rapid cooling during deposition inhibits element diffusion and makes Ti enrichment, which facilitates the formation of Ti_2Ni [43]. Afterward, due to the presence of O elements, Ti_2Ni precipitates convert partially to $Ti_4Ni_2O_x$ [102]. The strong overcooling caused by LPBF allows the Ti_2Ni to precipitate before the nucleation of the NiTi phase [103]. Then, the reaction and the dissolution of O elements induce the appearance of the $Ti_4Ni_2O_x$ phase. Next, the lenticular Ni_4Ti_3

precipitates disperse in NiTi SMAs prepared by SLM [40]. In this report, Ni_4Ti_3 precipitates were more equilibrated and stable under low E condition, as illustrated in Fig. 8 [40]. On the one hand, the lower E generated a larger supersaturation of Ni_4Ti_3 in the NiTi SMAs matrix and a lower nucleation barrier; therefore, the nucleation rate of grains rose. On the other hand, the high cooling rate and the low solute diffusion coefficient reduced the grain growth rate. Finally, other Ni-rich precipitates were transformed from Ni_4Ti_3 precipitates. For example, HEN et al [79] noticed that Ni_4Ti_3 precipitates in $Ni_{53}Ti_{47}$ SMAs fabricated by WAAM transformed into Ni_3Ti_2 and Ni_3Ti precipitates [104,105]. Except for the precipitates in NiTi SMAs, it is well known that they are related to the elemental species for Cu-SMAs and Fe-SMAs. For example, Cu_2ZrAl precipitates existed in CuAlNiMnCr SMAs [67], Cu_2TiAl precipitates appeared in CuAlNiTi SMAs [66], and $(Cu,Mn)_3Al_3Nd_4$ precipitates in CuAlMnNb SMAs [63]. Besides, FERRETTO et al [106] noted that the aging specimens developed precipitates with Cr and V elements.

There is a high density of dislocations in AM-fabricated SMAs [63]. ZHANG et al [107] noticed a high density of helical dislocations with an average dislocation density of up to $10^{11}\,cm^{-2}$ in SLMed NiTi SMAs. Helical dislocations were
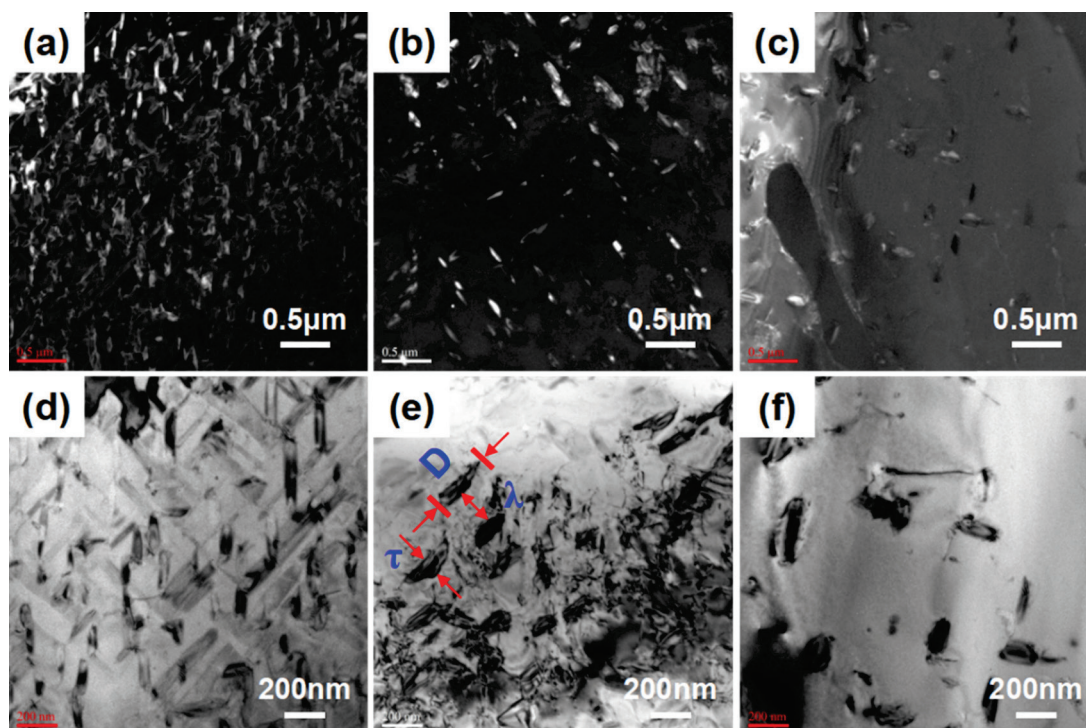

Fig. 8 TEM images of Ni_4Ti_3 with different E [40] (Copyright 2021, Elsevier)

formed due to the movement of bending dislocations in opposite directions and the thermal movement of vacancies. Moreover, the dislocation structure and density were changed significantly during the aging. In the study by MA et al [102], dislocation walls or tangles were formed as the aging time increased. Two main fields drive the dislocation motion; thermal activation to reduce the energy potential barrier and osmotic force generated by vacancy subsaturation in the Ni_4Ti_3 precipitates. There are two primary perspectives on the causes of dislocation formation. Considering the AM process, the development of dislocations with high density during AM is attributed to non-equilibrium rapid solidification and significant residual thermal stresses [39]. In terms of material properties, the high concentration of vacancies is the basis of dislocation occurrence.

Twins are usually observed in AM-fabricated SMAs. The common twinning styles are $\{1\bar{1}1\}$ type I twin, $\langle 011 \rangle$ type II twin and compound twin. Most studies attribute the twin formation to residual stresses during the AM fabrication process [39,63]. The large strain arises from the constraint of the parent phase on the new phase during the formation of martensite. Subsequently, twins emerged to regulate the strain [64]. ZHANG et al [107] revealed the reasons for various twin generations deeply in SLM-fabricated NiTi SMA. Elastic interactions related to the precipitation phase stress field during martensite phase transformation lead to $\{1\bar{1}1\}$ type I twin. Compound twins are dependent upon temperature gradients, precipitation, and twinning shear. It is essential that the generation of twins is accompanied by lattice distortion and stress field formation, which resists martensite deformation [39].

There are stacking faults in AM-possessed SMAs. The cause of stacking faults generation is a hot topic of concern. The inevitable factor is the unique thermal cycling effect during the printing process [64]. The solidified layer is thermally influenced to melt again, leading to an increase in stacking faults and a decrease in orderliness. Stacking faults are usually detected around the precipitates [106]. On the one hand, the lattice and thermal mismatch between the precipitate and the substrate triggers the formation of stresses. On the other hand, the precipitation-induced chemical composition change reduces the stacking faults

energy. However, stacking faults are also introduced in the absence of precipitates. KIM et al [68] dedicated that they were caused by phase boundaries, low-angle boundaries, and high-density dislocations in Fe−17Mn−5Si−10Cr−4Ni SMA built by LPBF. Accordingly, high residual stress, precipitation, and dislocation are the main reasons for stacking fault formation.

Table 3 summarizes the main features of precipitate, dislocation, twin and stacking fault in AM-ed SMAs. The results of studies on microstructure hold that precipitates, dislocations, twins, and stacking faults affect the phase transformation process and properties of SMAs together through sophisticated connections rather than acting individually.

Table 3 Main features of precipitate, dislocation, twin and stacking fault in AM-ed SMAs

Microstructure	Feature
Precipitate	Correlate with element types
Dislocation	Because of rapid solidification and large residual thermal stress
Twin	Affected by precipitates and residual stress
Stacking fault	Caused by residual stress, precipitate and dislocation in Fe-SMAs

3.4 Phase transformation

The phase transformation behavior of AM-fabricated SMAs is investigated, as listed in Table 4. The alloy at equilibrium state has been revealed to consist of solid solution and precipitate phases. However, the composition and scanning parameters considerably influence the phase transformation behavior. The phase transformation behavior of different types of SMAs (NiTi-SMA, Fe-SMA, and Cu-SMA) is discussed in detail.

(1) Firstly, in addition to the B_2 phase and $B_{19'}$ phase [49], NiTi-SMAs also possess R phase [79]. ZHAO et al [47] prepared NiTi SMAs at low energy density (375 J/mm^3) and observed two exothermic peaks during cooling. These implied two transformation types of the B_2 phase→R phase and the R phase→$B_{19'}$ phase. There are two possible reasons for this two-step transformation: the R-phase nucleation potential is lower than that of the martensite, and the composition of the matrix is inhomogeneous. Since the R-phase transformation

Table 4 Phase compositions of AM-fabricated SMAs

SMA	Composition	Ref	SMAs	Compositions	Ref
$Ni_{50}Ti_{50}$ (wt.%)	$B_{19'}+B_2+Ti_2Ni+Ni_3Ti$	[33]	$Ni_{50.8}Ti_{49.2}$	B_2	[60]
$Ni_{50.2}Ti_{49.8}$ (at.%)	$B_{19'}+B_2+(Ti_2Ni)$	[39]	$Ni_{55}Ti_{45}$ (at.%)	$B_{19'}+B_2+Ni_4Ti_3$	[71]
$Ni_{50.4}Ti$ (at.%)	$B_{19'}+B_2+Ni_4Ti_3$	[40]	$Ni_{50.93}Ti_{49.07}$	$B_{19'}+B_2+Ti_2Ni$	[72]
$Ni_{49.4}Ti_{50.6}$ (at.%)	$B_{19'}+B_2+Ti_2Ni$	[41]	$Ni_{50.93}Ti_{49.07}$	$B_{19'}+B_2+Ti_2Ni$	[73]
$Ni_{55.8}Ti$ (wt.%)	$B_{19'}+B_2$	[42]	$Ni_{50}Ti_{50}$ (wt.%)	$B_{19'}+B_2+Ti_2Ni$	[33]
$Ni_{50.4}Ti_{49.6}$	$B_{19'}+B_2+Ni_4Ti_3$	[43]	$Ni_{56}Ti$ (wt.%)	$B_2+Ti_2Ni+Ni_3Ti+Ni_4Ti_3$	[74]
$Ni_{50.6}Ti_{49.4}$	$B_{19'}+B_2$	[57]	$Ni_{50.6}Ti_{49.4}$ (at.%)	$B_{19'}+B_2+NiTi_2+Ni_4Ti_3$	[58]
$Ni_{50}Ti_{50}$ (at.%)	$B_{19'}+B_2+Ti_2Ni$	[44]	$Ni_{58}Ti_{42}$ (wt.%)	$B_2+Ni_4Ti_3+Ni_3Ti$	[75]
$Ni_{51.4}Ti$ (at.%)	B_2+R	[45]	$Ni_{50.7}Ti$ (at.%)	$B_{19'}+B_2$	[77]
$Ni_{50.8}Ti_{49.2}$ (at.%)	$B_{19'}+B_2$	[46]	$Ni_{50.7}Ti$ (at.%)	$B_{19'}+B_2$	[78]
$Ni_{50}Ti_{50}$ (at.%)	$B_{19'}+B_2+Ti_2Ni$	[47]	$Ni_{50.8}Ti_{49.2}$	$B_{19'}+B_2+R+Ti_2Ni$	[79]
$Ni_{55.98}Ti$ (wt.%)	$B_{19'}+B_2$	[48]	$Ni_{55.74}Ti$ (wt.%)	$B_{19'}+B_2+Ni_4Ti_3$	[80]
$Ni_{55}Ti_{45}$ (wt.%)	$B_{19'}+B_2$	[49]	$Ni_{52}Ti$ (at.%)	$B_2+Ni_4Ti_3$	[81]
$Ni_{49.4}Ti_{50.6}$ (at.%)	$B_{19'}+B_2+Ti_2Ni$	[50]	$Ni_{50.5}Ti$ (at.%)	$B_{19'}+B_2+R+Ni_4Ti_3$	[82]
$Ni_{50.4}Ti$ (at.%)	$B_{19'}$	[51]	$Ni_{50.9}Ti_{49.1}$	$B_{19'}+Ti_2Ni$	[83]
$Ni_{50.6}Ti_{49.4}$	$B_{19'}+B_2$	[52]	$Ni_{50.8}Ti$ (at.%)	B_2	[84]
$Ni_{55.4}Ti$ (wt.%)	$B_{19'}+B_2+Ni_4Ti_3$	[53]	$Ni_{50.4}Ti_{29.6}Hf_{20}$	$B_{19'}$	[61]
$Ni_{55.4}Ti$ (wt.%)	$B_{19'}+B_2+TiC$	[53]	TiNiCu	$B_{19'}+B_2$	[85]
$Ni_{50.8}Ti$ (at.%)	$B_{19'}+B_2$	[54]	TiNiCu	$B_{19'}+B_2$	[86]
$Ni_{49.9}Ti$ (at.%)	$B_{19'}+R$	[55]	NiTiTa	$B_{19'}+B_2$	[8]
$Ni_{50.73}Ti$ (at.%)	$B_{19'}+B_2$	[56]	NiTiCrMoNb	$B_2+Ti_2Ni+Cr_2Ti$	[7]
$Ni_{50.8}Ti_{49.2}$ (at.%)	$B_{19'}+B_2$	[59]	$NiTi\text{-}CeO_2$	$B_{19'}+B_2$	[62]
$Cu_{71.6}Al_{17}Mn_{11.4}$	β_3	[9]	CuAlNiMn	β'_1	[63]
CuZnAl	$\beta'+\alpha$	[64]	$CuAl_{13.5}Ni_4Ti_{0.5}$	β'	[66]
$FeMn_{17}Si_5Cr_{10}Ni_4$	$\delta+\gamma+\varepsilon$	[69]	CuAlNiMn	β'_1	[67]
$FeMn_{17}Si_5Cr_{10}Ni_4$	$\delta+\gamma+\varepsilon$	[68]	CuAlNiMnZr	β'_1	[67]
FeMnSiCrNi(V,C)	$\delta+\gamma$	[10]			

is associated with Ni_4Ti_3, the evaporation of Ni elements at high energy density (525 and 675 J/mm^3) reduces the precipitation of Ni_4Ti_3, which prompts the absence of the R phase. (2) E exerts the predominant function in altering the phase transformation behavior for Cu-SMA. XI et al [63] constructed Cu−11.85Al−3.88Mn−1.6Nb SMAs through SLM. The results suggested that when E was below 154 J/mm^3, β'_1 (18R) martensite became the dominant phase, accompanied by γ'_1 (2H) martensite; when E was 184 J/mm^3, γ'_1 martensite took the dominant role. This is provoked by the valence electron concentration (e/a) per atom in the alloy [108]. (3) Fe-SMAs held a complex phase transformation behavior owing to the phase transformation occurring during the AM process. FERRETTO et al [70] reported that almost the entire FCC-γ phase existed when E reached a maximum value of 194.44 J/mm^3. Nonetheless, the dominant phase was BCC-δ (98%), when the E descended to a minimum value of 63.89 J/mm^3. In another work, the addition of V/C elements to the Fe-SMAs matrix caused the FCC-γ phase [106]. This was correlated to the primary phase type and the ratio of Cr equivalent ($Cr_{eq}=Cr+1.5Si$) to Ni equivalent ($Ni_{eq}=Ni+0.31Mn+22C$) (when the ratio is less than 1.5, FCC-γ is the dominant solidified phase). Therefore, the phase transformation (from

BCC-δ to FCC-γ) during the production process is the main reason for the differences in phase composition.

Figure 9 summarizes the phase transformation temperatures (TTs) for different SMA systems processed by AM, represented by the starting temperature of martensite transformation (M_s). It can be known that TTs intensely vary with the element types and scanning parameters. For example, after Hf was doped with NiTi SMAs, the TTs increased to above 200 °C [109]. Besides, LU et al [87] and XU et al [62] obtained that La_2O_3 and CeO_2 promoted the formation of LaNi and NiCe, respectively. These caused an ascent in TTs. Concerning the scanning parameters, WANG et al [48] investigated TTs converted with P, V, and H in SLM-produced NiTi SMAs, as exhibited in Fig. 10. As the P rose from 60 to 200 W, the martensite transformation peak temperature (M_p) increased consistently from 265 to 285 K. When the V grew from 400 to 1200 mm/s, the M_p decreased monotonically from 294 to 262 K. As H increased from 40 to 110 μm, the M_p declined dramatically from 290 to 268 K. In this field, Refs. [39,42,45,91] also demonstrated similar results. GAN et al [40] concluded that the TTs in the NiTi SMAs fell significantly as E rose (from 37.88 to 46.30 J/mm³). Next, the TTs showed an upward trend between 46.30 and 79.37 J/mm³. Finally, the TTs dropped slightly when E increased to 104.17 J/mm³. Overall, there was a positive correlation between the characteristic temperature and E. Apart from the influence of grain size, the compositional inhomogeneity can induce these phenomena (because of the evaporation of Ni elements). Notably, the reasons for inhomogeneous composition are evaporation of elements, burnout of elements, and formation of precipitates. For example, the change in TTs for CuAlMn and CuAlMnNb SMAs is attributed to the burnout of Mn elements and martensite nucleation at grain boundaries [110]. For CuZnAl SMAs, the α precipitation made the content of Zn and Al elements rise in the matrix [111], which resulted in a descent in TTs. Additionally, WANG et al [81] analyzed the reasons for the increase in TTs from perspectives of the elastic disturbance field generated around the Ni_4Ti_3 precipitates (internal stress) and the residual stress generated by AM (external stress). Compared to the role of internal

stress, FENG et al [112] suggested that the effect of dislocations is more dominant, and thus the joint action of the two has a slight inhibitory effect on the phase transformation.
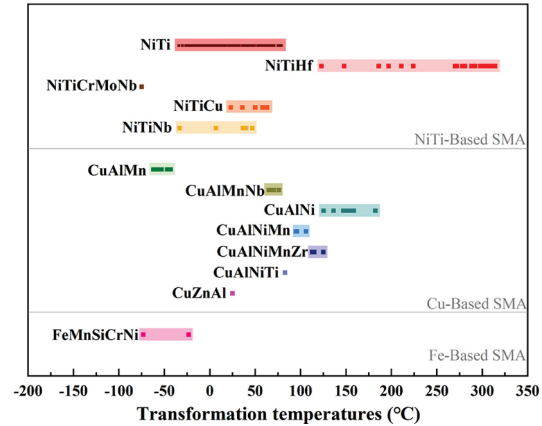

Fig. 9 Phase transformation temperatures of different AM-ed SMAs (NiTi-based SMAs: B$_2$→B$_{19'}$; Cu-based SMAs: Austenite→β'_1 (CuZnAl: Austenite→β'); Fe-based SMAs: γ→ε)

Based on the above findings, the multiple factors influencing the phase transformation of SMAs are summarized: (1) The TTs are highly dependent upon the elemental content. A 1% decrease in nickel content in the matrix is generally believed to result in a 100 °C increase in M_s [101]. Therefore, once the behavior of altering the elemental content is triggered (such as the evaporation and burnout of elements during AM), the TTs are modified. (2) Grain size affects the TTs, because the decrease in grain size and the ascent in grain boundaries inhibit the phase transformation, which results in a fall in the TTs. It is worth noting that the fine grains suppress the martensite transformation in NiTi alloys, but only when the grains are in the nanoscale. (3) Besides the volume fraction and the morphology of precipitates, the precipitation−substrate interface has a complex effect on the phase transformation process. Firstly, the volume fraction of precipitates affects the elemental content of the matrix, and thus the TTs are changed. Secondly, the nucleation energy rises when the size of precipitate and the interparticle distance is small, leading to a descent in the M_s. Finally, the atomic mismatch between the precipitate and the matrix varies the internal stress, which contributes to increase of the TTs [113]. (4) Dislocations affect the phase transformation.
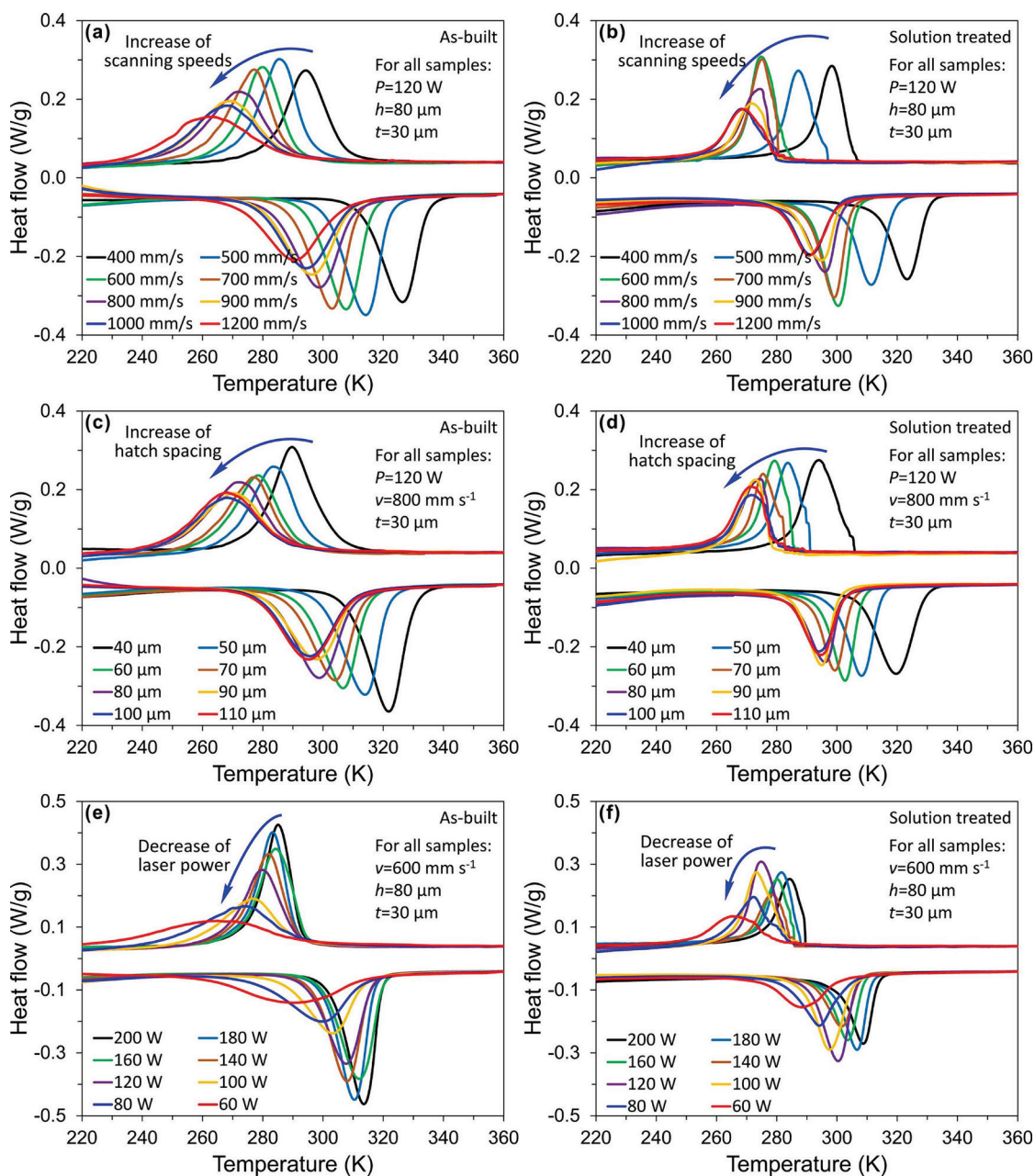
Fig. 10 Phase transformation behavior of NiTi SMAs printed by SLM: (a, b) As-built and solution-treated specimens with different V from 400 to 1200 mm/s; (c, d) As-built and solution-treated specimens with different H from 40 to 110 μm; (e, f) As-built and solution treated samples with different P from 60 to 200 W [48] (Copyright 2020, Elsevier)

The presence of dislocations prompts martensite nucleation, but excessive dislocation boundaries hinder the growth of the martensite variants. (5) Residual internal stresses facilitate phase transformation (non-major factor). Usually, the combined effect of microstructure (the above five influencing factors) modifies the phase transformation, so a variety of factors should be considered when understanding and regulating the phase transformation behavior.

4 Properties of SMAs by additive manufacturing

With the growing popularity of AM, the characterization of the performance of AM-processed SMAs is carried out in order to assess their viability as structural components. The rapid solidification of the AM process may enhance the performance. However, it is impeded by the

presence of defects. In this section, four aspects of tensile and compressive properties, shape memory effect (SME), superelasticity effect (SE), and elastocaloric effect are discussed. And the methods of combining microstructures to facilitate properties are revealed.
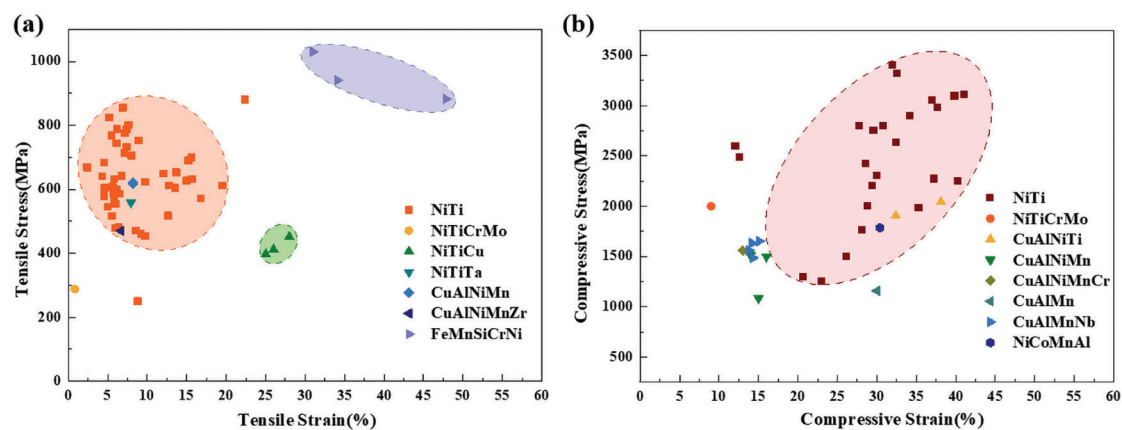
4.1 Tensile and compressive properties

Figure 11 summarizes the relationship between tensile or compressive stress and strain of AM-prepared SMAs. It can be noticed that for the exact composition of the alloy, the properties vary enormously in a particular range, determined by the microstructure and the phase transformation behavior. Therefore, different scanning parameters or sampling locations can be used to adjust the microstructure of SMAs, such as grains, precipitates, and dislocations, which can further affect the phase transformation behavior and improve the tensile and compressive properties.

The tensile and compression curves exhibit the typical double-yielding behavior. It is divided into four stages: Stage I is elastic deformation, Stage II is stress-induced martensite transformation or martensite reorientation, Stage III includes elastic deformation of reoriented martensite, and stage IV means the plastic deformation of martensite. Among them, Stage II is determined by the initial state (austenite or martensite) before loading. When SMAs are loaded, the critical stress σ_{SIM} (the plateau stress) inducing martensite transformation or reorientation is associated with the phase transformation temperature [48]. The negative correlation between the two is analyzed by the Clausius-Clapeyron equation [42]:

$$\frac{\mathrm{d}\sigma_c}{\mathrm{d}M_s} = -\frac{\Delta H}{T_0 \varepsilon_0} \tag{1}$$

where σ_c is the critical stress, M_s means the martensite transformation starting temperature, ΔH represents the enthalpy of transformation per unit volume, T_0 implies the phase equilibrium temperature of the matrix and martensite, and ε_0 is the axial component of transformation strain. This relationship was demonstrated in the study of FU et al [97], who provided that σ_{SIM} (approximately 1200 MPa) increased as M_s declined (the Ti-rich second phase suppressed the martensite transformation). However, the macroscopic and microscopic deformation stages are not completely consistent. MA et al [52] divided the deformation process of LPBFed-Ni$_{50.6}$Ti$_{49.4}$ SMAs into four stages from microstructure, including (1) B$_2$ phase dominant stage, (2) reversion stage, (3) Balance phase, and (4) B$_{19'}$ phase dominant phase. In addition, a distinct phase transformation plateau may not be noticed during loading. LI et al [76] suggested that the phenomenon was caused by the plastic deformation of austenite and martensite transformation occurring almost simultaneously.

The fine microstructure in AM-fabricated SMAs enhances the tensile and compressive strength. For example, LU et al [39] observed an ascent in tensile yield strength ($\sigma_{0.2}$=(477±10) MPa), the critical stress-induced martensitic phase transformation strength (σ_c=(565±18) MPa), and ultimate tensile strength (σ_{UTS}=(788±20) MPa) of SLM-processed NiTi SMAs compared to the conventional casting specimens. Besides, the compressive fracture strain declined slightly by

Fig. 11 Mechanical properties of different AM-ed SMAs: (a) Tensile stress vs tensile strain; (b) Compressive stress vs compressive strain (at as-fabricated state) [7−9,13,39,41,50,51,67,70,76,77, 80−82,90,99,101,107]

around 2.2% and the tensile fracture strain by around 1.9%. This is due to the high cooling rate that retains the sizeable residual stress and then facilitates martensite transformation [94]. Afterward, the high density of dislocations and fine microstructure lead to the higher fracture strength and lower fracture strain of NiTi SMAs.

The effect on tensile and compressive properties was explicitly reviewed in terms of scanning parameters and sampling locations. Firstly, XIONG et al [114] compared the tensile properties of NiTi SMAs with different P (20−60 W). They concluded that the samples at lower P exhibited higher stresses at the same strain. This is due to the more austenite phases, which means that higher stress is required to promote martensite transformation. As P ascended, the fracture strength fell, owing to the larger grains. Furthermore, the strength of SMAs does not satisfy the linear law with E. Figure 12 demonstrated that with the increase of E (37.88−99.21 J/mm^3), there was a fluctuating trend in the strength of SLM-built NiTi SMAs during compression and tension [40]. During the tensile process, SMAs with E at 55.56 J/mm^3 held high ultimate strength and elongation (801.7 MP and 7.64%). For low E (40−60 J/mm^3), the interactions between Ni$_4$Ti$_3$ precipitates and massive dislocations resulted in excellent mechanical properties. However, the coherence between larger Ni$_4$Ti$_3$ precipitates and the NiTi matrix was disrupted, and the stress field around the precipitates was gradually weakened, thus losing the potential for the precipitation strengthening. In addition, LI et al [76] reported σ_{SIM} of 293.2 MPa, tensile strength of 578.9 MPa, and elongation of 4.52% for NiTi SMAs along the building direction.

However, the σ_{SIM}, tensile strength, and elongation were 187.8, 599.5 MPa, and 6.09%, respectively, when the tensile direction was perpendicular to the building direction. The differences in the above properties are ascribed to the effect of textures on martensite transformation. Specifically, the columnar grains with $\langle 001 \rangle$ orientation are detrimental to stress-induced martensite transformation [115] (building direction), and the equiaxed grains provide more strain compatibility, which promotes the formation of stress-induced martensite (horizontal direction).

In summary, the tensile and compressive properties of SMAs depend strongly on the microstructure. Specifically, fine grain strengthening, dislocation strengthening and precipitation strengthening are the major methods. Moreover, the phase composition and texture are also necessary factors. Therefore, to achieve SMAs with high tensile and compressive properties, the microstructure can be adjusted by changing the scanning parameters and sampling locations.

4.2 Shape memory effect and superelasticity effect

AM-fabricated SMAs present excellent and stable shape memory effects. FENG et al [59] proposed that 100% shape recovery of NiTi SMAs could be achieved with deformation up to 10%. The appearance of the R phase is reported to facilitate the SME. Specifically, the R phase and martensite experience reorientation during the deformation process, and then the transformation processes of B$_{19'}$→R and R→B2 phase occur during the heating process to gain SME. LU et al [39] immersed NiTi SMAs in ice water and bent them to various angles
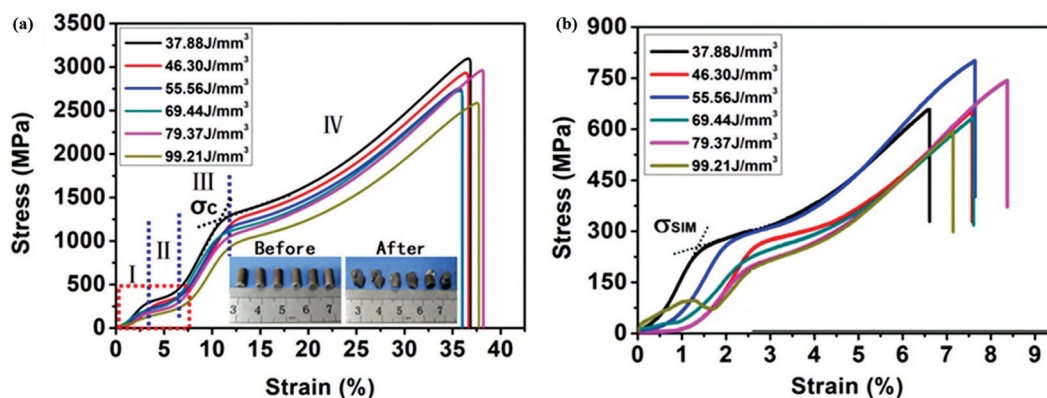

Fig. 12 Effect of different E on mechanical properties of SLM-ed NiTi SMAs: (a, b) Compressive stress−strain curves; Tensile stress−strain curves [40] (Copyright 2021, Elsevier)

(45°−360°) and then proved that they automatically recovered their shapes in hot water. The recovery rate of all specimens reached 100% at strains ranging from 0.53% to 4.19%. In addition, for Cu-SMAs, the SLM-built Cu−11.85Al−3.88Mn−1.6Nb obtained by XI et al [63] possessed 99.26% recovery and 5.32% shape memory strain. For Fe-SMAs, the recovery strain of conventionally fabricated Fe−17Mn−5Si−10Cr−4Ni−1(V,C) was 1.15%. However, LPBF-prepared samples held better SMEs with a maximum recovery strain of 1.64%.

The SME depends on the microstructure characteristics; therefore, it can be modulated by altering the scanning parameters. The influence of processing parameters on the recovery rate or recovery strain of SMAs is attributed to the variation of densities, grain orientation, and precipitation. FENG et al [112] found that the shape memory recovery rate of NiTi SMAs showed a fluctuating trend as H increased (50−170 μm). The best performance of NiTi SMAs at H=110 μm was associated with the lowest porosity (0.04%). For Fe-SMAs, FERRETTO et al [10] observed that the

recoverable strain increased from 0.12% to 0.39% with rising V. This phenomenon is caused by three reasons: (1) At low V, the high ferrite content affects the transformation between the ε and γ phases, thus reducing the possibility of martensite formation. (2) At high V, the grains with a stronger $\langle 001 \rangle$ orientation promote martensite transformation. Furthermore, Fig. 13 demonstrated that the recoverable strain of NiTi SMAs rose to 4.99% as E decreased to 155 J/mm³ [41]. It is noteworthy that the recovery rate of the alloy was maximized to 98.7% at the E of 222 J/mm³ (the optimal SME). This is caused by the grain boundaries and precipitates that inhibit the formation and movement of dislocations and thus facilitate martensite transformation. Similar results are shown for Cu SMAs. For example, XI et al [63] argued the SME for E in the range of 123−185 J/mm³ and identified that the sample with E of 154 J/mm³ presented the most considerable recoverable strain when it was loaded to 6%.

In addition, AM-prepared SMAs demonstrate a remarkable superelasticity effect (SE). For NiTi-SMAs, FENG et al [59] observed that >90%
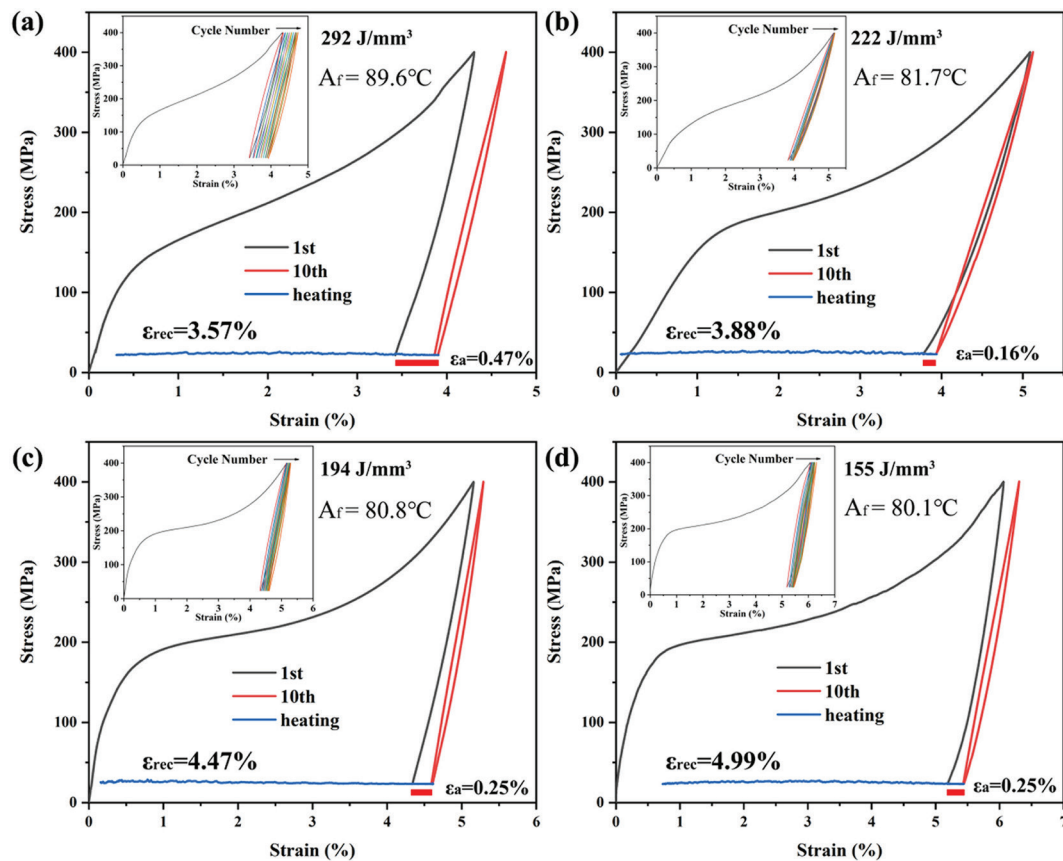

Fig. 13 Effect of different E on SME: (a) 292 J/mm³; (b) 222 J/mm³; (c) 194 J/mm³; (d) 155 J/mm³ [41] (Copyright 2019, Elsevier)

deformation recovery rate could be attained for a pre-strain of less than 8%. Further, WAN et al [60] achieved a superelastic recovery strain of 9.2% for NiTi SMAs with the LSF method. It is noteworthy that the AM technique enhances the recoverable strain of SMAs compared to conventional methods. For example, the maximum recoverable strain of $Cu_{71.6}Al_{17}Mn_{11.4}$ slightly increased from 2.46% (for cast samples at 4% strain) to 2.86% (for SLM-ed parts at 5% strain) [9], ascribed to the fine grain size in the LPBF process. Likewise, the recoverable strain of Fe-SMAs grew to 1.64%. FERRETTO et al [70] explored that the rise in SE was attributed to the interaction between the boundary and the hcp-ε phase.

SE is closely associated with the scanning parameters and the sampling location. Ehsan SAGHAIAN et al [98] dedicated that lower H enabled NiTi SMAs to show higher strain recovery (up to 90%) and more stable superelastic response. ZHUO et al [64] described that the irrecoverable strain of CuZnAl SMAs presented a fluctuating trend (3.46%, 2.87%, 3.15%, 3.54%, and 4.43%) with enhancing E (79.4, 99.2, 119.0, 208.3, and

$324.1 \ J/mm^3$). Initially, the parent phase was retained during solidification, and then reversible martensite content was reduced (due to the evaporation of Zn elements), which resulted in the change of the irrecoverable strain. In addition, LI et al [76] noted that NiTi SMAs along horizontal orientation possessed higher recovery rates (more than 80%) than those along the building orientation during ten tensile cycles. Columnar grains with $\langle 001 \rangle$ orientation along the building direction are unfavorable for SE. In contrast, equiaxed grains offer more strain compatibility, which promotes phase transformation. Similar characteristics were detected by ZHANG et al [101] in this aspect. Figure 14 illustrates that at the 25th cycle, the recovery rates of the horizontal and vertical NiTi SMAs gradually reduced from 98.62% and 97.44% to 94.93% and 90.75%, respectively. The low martensite content and dislocation density after deformation in the horizontal direction cause excellent SE.

Table 5 summarizes SME and SE reported for AM-ed SMAs. The same essence of SME and SE is phase transformation. Therefore, the effect of
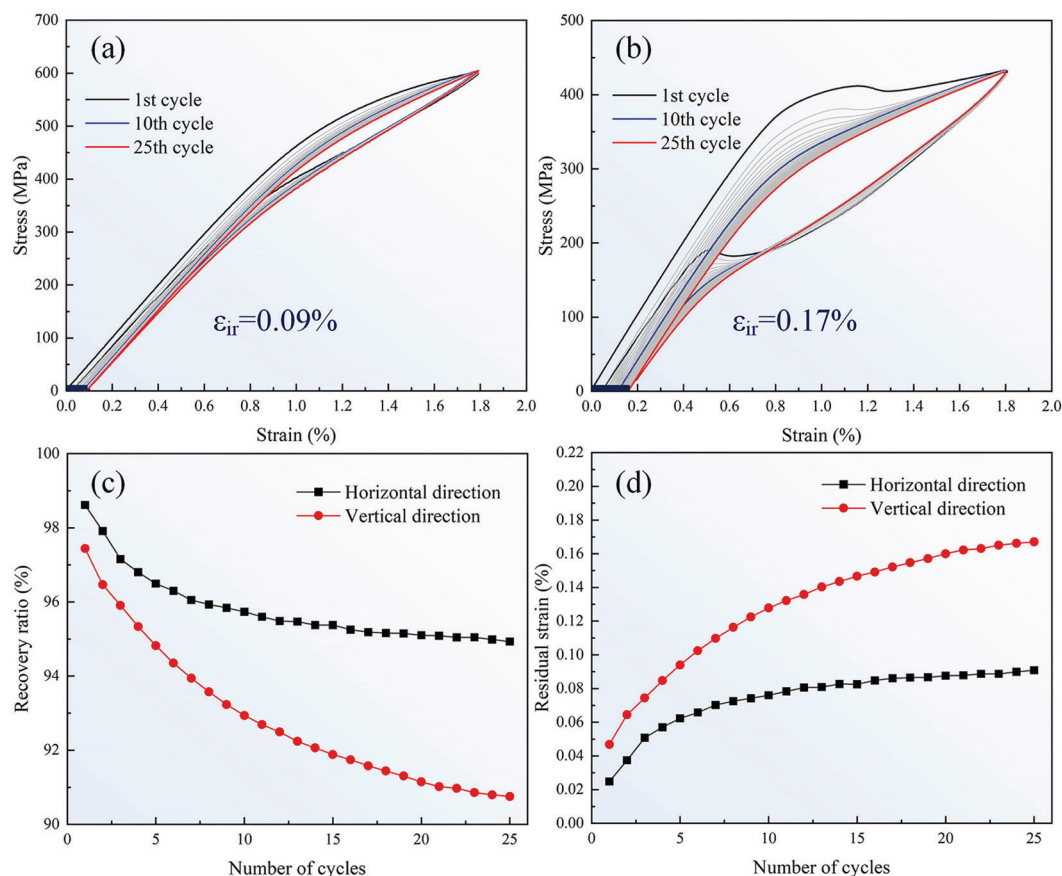
Fig. 14 SE of NiTi SMAs built by WAAM: (a, b) Tensile strain−stress curves of samples with horizontal and vertical directions; (c, d) Effects of number of cycles on recovery ratio and residual strain [101] (Copyright 2022, Elsevier)

influencing factors (grains, dislocations, precipitates, twins, and stacking faults) on SME and SE is revealed together. First, fine grains improve the ability of dislocation slip, which can reduce the accumulation of stress concentration and plastic deformation and thus increase the residual strain. In addition, a great number of grain boundaries serve as nucleation sites [9,84] and inhibit the formation and movement of dislocations [39], contributing to the occurrence of transformation. However, columnar grains are easily activated during deformation, which is not conducive to stress-induced martensite transformation (reduce the martensitic critical stress [99]), and therefore there are adverse effects SE [76,101]. Secondly, dislocations generated during deformation stabilize the martensite variant and martensite does not transform to austenite during heating, thus against SME and SE. Then, the relationship between precipitations and properties is more sophisticated.

Table 5 Summary of SME reported for AM-ed SMAs

Property	SMA	ε/%	σ/MPa	Recovery strain/%	Recovery ratio/%	Ref.
SME	$Ni_{50}Ti_{50}$ (wt.%)		1150	6.17		[33]
	$Ni_{50.6}Ti_{49.4}$		1000	6.8		[52]
	$Ni_{50.8}Ti_{49.2}$ (at.%)	1.8			98.62	[101]
	$Ni_{50.4}Ti_{49.6}$		550	2.58		[43]
	$Ni_{52}Ti$ (at%)		700	2.96	57.28	[81]
	$Ni_{51.4}Ti$ (at.%)		960	4.6		[45]
	$Ni_{50.5}Ti$ (at.%)	6		1.13	100	[82]
	$Ni_{50.8}Ti_{49.2}$	14		6.1	91.8	[59]
	$Ni_{55.78}Ti$ (wt.%)	2		1.4	70	[76]
	$Ni_{50.8}Ti$ (at.%)	2		0.3		[34]
	$Ni_{50.8}Ti_{49.2}$	10		9.2		[60]
	$Ni_{50.8}Ti$ (at.%)	4		3.07		[84]
	$Ni_{50.8}Ti$ (at.%)	6		4.25	70.83	[116]
	$Ni_{50.7}Ti$		1000	10.56	55.78	[78]
	$Ni_{50.8}Ti_{49.2}$ (at.%)		800	5.39	86.52	[98]
	CuZnAl	9		6.13		[64]
	$Cu_{71.6}Al_{17}Mn_{11.4}$ (at.%)	4			65.3	[9]
	$FeMn_{17}Si_5Cr_{10}Ni_4(V,C)_1$	2		0.80		[10]
	Fe–Mn–Si–Cr–Ni-(V,C)	4		0.64		[106]
SE	$Ni_{55.8}Ti$ (wt.%)		400		76.1	[42]
	$Ni_{50.8}Ti_{49.2}$ (at.%)	7		4.4		[94]
	$Ni_{50.9}Ti$ (at.%)	8			98	[112]
	$Ni_{50}Ti$ (at.%)	6		5.17		[47]
	$Ni_{50.81}Ti_{49.19}$ (at.%)	6			72	[114]
	$Ni_{49.4}Ti_{50.6}$ (at.%)		400	5.32		[43]
	$Ni_{50.7}Ti$		347.48	1.15		[78]
	$Ni_{50.4}Ti$ (at.%)	8			58	[51]
	Cu−11.85Al−3.99Mn−1.64Nb	8		5.29		[63]
	$FeMn_{17}Si_5Cr_{10}Ni_4$ (wt.%)	5.26		3.77		[68]

ε and σ are maximum strain and maximum stress, respectively

On the one hand, fine precipitates act as pinning points to block the martensite transformation, thus reducing SE [106]. On the other hand, the stress/strain field around precipitates prevents dislocation motion which is favorable to SME and SE. Notably, this role of hindrance is associated with the size of the precipitate. For example, the stress/strain field is maximum for Ni_4Ti_3 precipitates with aspect ratio of 1 (spherical) [43]. In addition, precipitations vary the matrix element content, which exerts an influence on the phase transformation. Next, the ascent in the number and width of twins during deformation leads to severe dislocation pile-up. The composite twin variants remain after unloading, which is disadvantageous to the SE [77,78]. Finally, the high density of stacking faults present plenty of nucleation sites, which enhances the SME and SE. Especially in Fe-SMAs, stacking faults promote the formation of ε-phase and phase transformation. Based on these, the effective methods to elevate SME and SE are summarized as follows: (1) From the perspective of element contents, the evaporation or precipitation of elements in the manufacturing process affects the phase transformation, so adjusting the element content can effectively improve SME and SE. For example, increasing the Ni content in NiTi-SMAs can reduce the TTs and thus elevate the SE. (2) Concerning the grain, changing the scanning strategy or sampling method provides opportunities for facilitating SME and SE. (3) Considering precipitates, dislocations, twins, and stacking faults, heat treatment can be employed to eliminate residual thermal stresses and induce favorable structure formation to obtain SMAs with exceptional SME and SE.
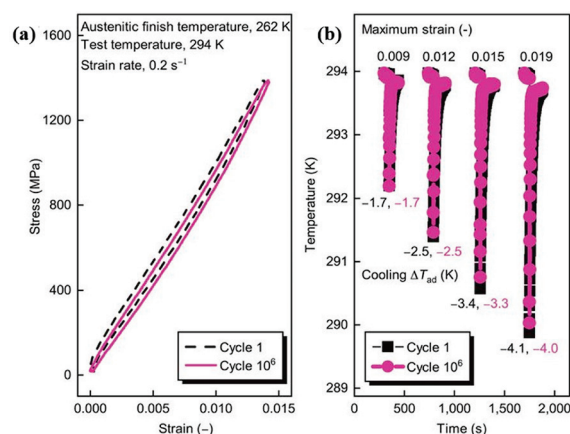
4.3 Elastocaloric effect

The stress-induced martensite transformation can induce elastocaloric effects in SMAs. This extremely significant self-cooling behavior plays a decisive role in the development of solid cooling technology. The goal of research in this area is to fabricate high-efficiency and low-hysteresis elastocaloric cooling materials by means of AM technology.

The present research is limited to NiTi-SMAs. WAN et al [60] found that the adiabatic temperature changes (ΔT) of LSF-printed $Ni_{50.8}Ti_{49.2}$ during

unloading were −6.3, −12.6, −16.6, and −18.6 K, respectively (at strains of 4%, 6%, 8%, and 10%). It was demonstrated that there were correlations between ΔT and the volume fraction of austenite. In Ref. [117], the generation of the elastocaloric effect was attributed to precipitates. Specifically, the Ti_2Ni precipitates presented an aspect ratio of about 15 and a volume fraction close to 20%, which enabled SMAs to withstand the load in elastic deformation, consequently leading to a narrow hysteresis. In a subsequent study [118], they further verified the contribution of precipitates to the elastocaloric effect of SMAs. They added the non-transformed intermetallic Ni_3Ti phase in NiTi SMAs through the LDED process. As illustrated by stress−strain curves in Fig. 15, the SMAs held quasi-linear behavior, and the hysteresis was dramatically reduced. Remarkably, they possessed stable mechanical properties and elastocaloric response over 10^6 cycles. In Ref. [45], it was also confirmed that the elastocaloric effect could be adjusted by switching the processing parameters (H=0.6 mm or 0.8 mm). The thermoelastic effect is related to the stress-induced isothermal entropy change (ΔS_{iso}). Calculated by the following equation, the ΔS_{iso} at 4% strain was 34.9 J·kg^{-1}·K^{-1}) (at 333 K):

$$\Delta S_{iso} = \frac{1}{\rho} \int_0^\varepsilon \left(\partial \sigma / \partial T \right)_\varepsilon \, d\varepsilon \qquad (2)$$

where ρ is the density. It was the large entropic change that caused the thermoelastic effect of NiTi SMAs. Moreover, latent heat is considered a

Fig. 15 Stability of elastocaloric effect: (a) Compressive stress−strain curves; (b) Elastocaloric cooling in different strains [118] (Copyright 2019, American Association for Advancement of Science)

necessary parameter. According to $\Delta T=\Delta H_{M-A}/C_p$ (ΔH_{M-A} is the latent heat of endothermic transformation, and C_p is the specific heat capacity), the maximum latent heat of NiTi was more than 30 J/g and thus, in principle, can produce the ΔT up to 54 °C [117].

Table 6 summarizes the elastocaloric effect reported for AM-ed SMAs. Overall, the large latent heat ΔH, entropy change ΔS, and low hysteresis enable SMAs to develop superb elastocaloric effect. Since the elastocaloric effect occurs above A_f, this property depends on the factors modifying the phase transformation temperature. The practical methods to refine the elastocaloric effect are as follows: (1) Reduce the grain size and thus enhance the yield strength; (2) Introduce uniform precipitates through aging treatment to achieve precipitation strengthening; (3) Regulate alloy composition or heat treatment to increase latent heat.

Table 6 Summary of elastocaloric effect reported for AM-ed SMAs

SMA	$\varepsilon/\%$	$\sigma/$ MPa	Temperature/ K	$\Delta T/$ K	Ref.
$Ni_{51.4}Ti$ (at.%)		600	333	23.2	[45]
$Ni_{51.4}Ti$ (at.%)		600	295	18.4	[45]
$Ni_{51.4}Ti$ (at.%)		800	295	17.2	[45]
$Ni_{50.8}Ti_{49.2}$	4		298	6.3	[60]
$Ni_{50.8}Ti_{49.2}$	6		298	12.6	[60]
$Ni_{50.8}Ti_{49.2}$	8		298	16.6	[60]
$Ni_{50.8}Ti_{49.2}$	10		298	18.6	[60]
$Ni_{51.5}Ti_{48.5}$	0.9		298	1.7	[118]
$Ni_{51.5}Ti_{48.5}$	1.2		298	2.5	[118]
$Ni_{51.5}Ti_{48.5}$	1.5		298	3.4	[118]
$Ni_{51.5}Ti_{48.5}$	1.9		298	4.1	[118]
NiTi	3		395	4.2	[117]
NiTi	4		395	6.2	[117]
NiTi	5		395	7.5	[117]
NiTi	6		395	6.7	[117]

5 Perspectives

5.1 Research direction

According to the development of AM-ed SMAs, future research directions are proposed focusing on four aspects: material, technology, property, and method.

Up to now, AM has been employed to create a wide variety of SMAs. However, to satisfy complicated service conditions (high temperature, low temperature, marine environment, vibration conditions, etc), more novel SMAs need to be developed, such as ZrCu SMA, Ti-based SMA, and Co-based SMA. It is remarkable to note that the purity of the raw material (powder and wire) is the basis for achieving excellent SMAs. For instance, carbon and oxygen elements introduced during the printing process can react with metallic elements, thus modifying the phase transformation temperature. Therefore, reducing the content of impurity elements in the raw material is crucial. Besides the quality of the raw material, the substrate applied to production is exceptionally significant. For example, unsuitable substrate materials can generate cracks in SMAs. Above all, the compatibility between advanced materials and technologies must be explored in depth.

Varying scanning parameters and scanning strategies are capable of modulating the microstructures and properties of SMAs. Therefore, most works have been carried out to achieve a high relative density of SMAs with optimal parameters. The reliability (density, geometric accuracy, homogeneity, etc) and reproducibility of the productions also require further investigation. More significantly, the complex thermal behavior during the AM process generates residual stresses, which can seriously deteriorate the mechanical properties. Therefore, relevant solutions should be proposed to eliminate the residual stresses. In addition, the mixing printing technology is considered a possible research direction. Materials with different characteristics are assembled in one part to realize unique functions. Incidentally, the establishment of in-situ inspection methods during the printing process enables monitoring potential problems, such as powder distribution and melt pool solidification behavior. These provide an effective means to understand the metallurgical mechanisms and optimize the printing technology.

Current studies on the performance of AM-fabricated SMAs have been concentrated on mechanical properties, SME, and SE, while those on functional properties such as fatigue behavior,

corrosion resistance, damping properties, bio-compatibility, and friction properties are limited. Special attention should be paid to these properties, which enhances the availability of SMAs. And AM builds SMAs with complex geometries, which may dramatically expand the application range. Additionally, it is worth mentioning that heat treatment can alter microstructures to obtain the desired properties. Therefore, regulating the temperature and time in heat treatment is a necessary research direction.

For the AM-processed SMAs, numerous researches are mainly conducted by experimental means. In fact, many simulation methods can be used to address related problems. These numerical simulation approaches consider fluid flow, heat transfer, and phase transformation. For example, the E-T model can effectively predict the defect types for different process parameters; based on the finite element analysis model, melt pool characteristic, deposition rate, and stress field can be captured. However, the precise simulation of properties and functionalities is lacking in this regard. Therefore, a model combining material, process, performance, and function is exploited in the promising research field.

5.2 Application prospect

SMAs with porous structures fabricated via AM are considered competitive materials which have the possibilities to be utilized in diverse fields. First, in the aerospace area, MCCUE et al [119]

produced hinges of the NiTi SMA by SLM and successfully simulated solar panel arrays, as illustrated in Fig. 16. In their work, the deformed hinges were able to recover to a planar state under the effect of heating. When employed in a solar panel array, the four-panel and the nine-panel array unfolded smoothly, effectively reducing the cross-sectional area by 75%−95%. This study demonstrated theoretical evidence for SMAs to control deployable structures. In addition, XU et al [120] prepared NiTi SMAs with a honeycomb structure, which can be applied to smart deformable wings with a good in-plane tensile deformation capability. Then, in the biomedical field, ZHAO et al [121] produced NiTi SMAs with Menger sponge-like structures, which possessed various fractal dimensions and fractal orders. The maximum compressive stress and elastic modulus of the alloys reached (16.93 ± 1.75) MPa and (0.59 ± 0.11) GPa, respectively, at a strain of 3% (D=2.35, and N=3). These are nearly the same features as those of human cancellous bone. These findings illustrated the feasibility of porous alloys as metallic implants. Remarkably, there is great potential for customizing scaffolds and related structures are shown in Fig. 17. Finally, AM-built SMAs with truss structures could be implemented as actuators, which indicated high stiffness and force. In conclusion, AM-fabricated SMAs possess a vast application prospect. It is hoped that their mass production in various industries can be achieved.
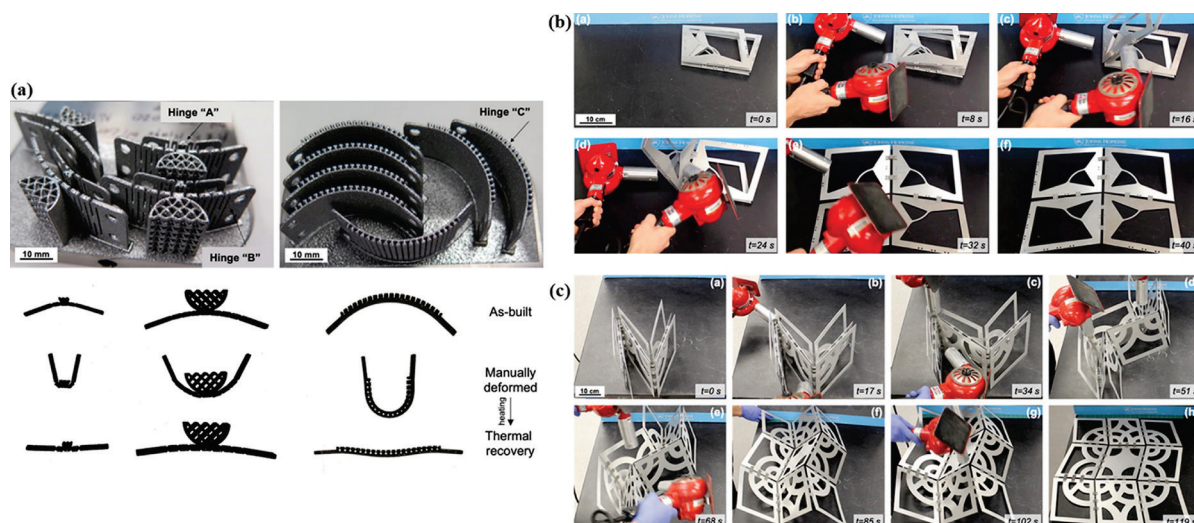
Fig. 16 SMAs applied to aerospace applications: (a) SLM-printed NiTi hinges; (b) Time series of four-panel arrays; (c) Time series of nine-panel arrays [119] (Copyright 2021, Elsevier)
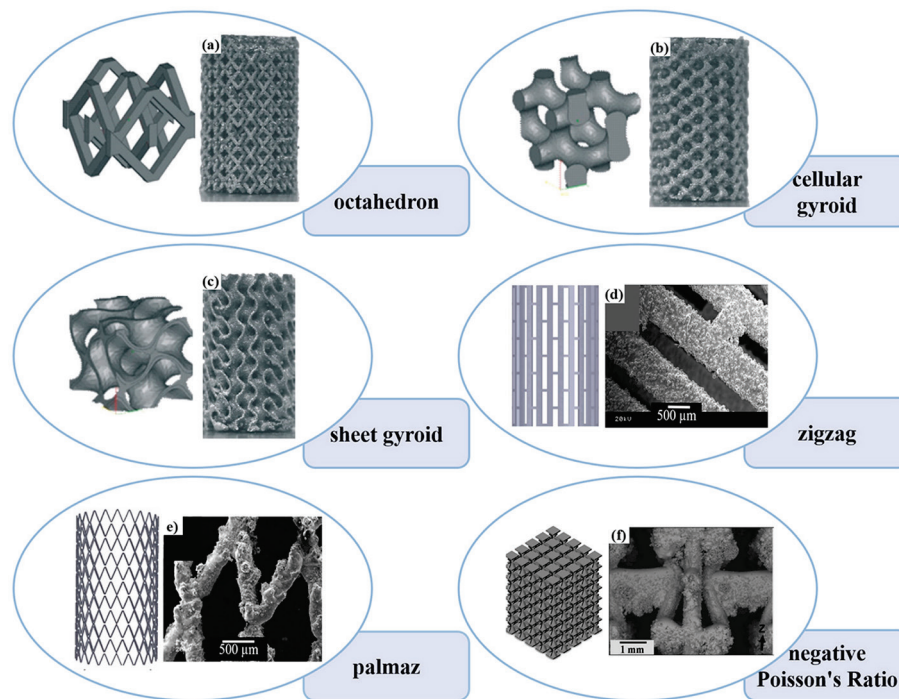
Fig. 17 Multifarious structures produced with SMAs by AM: (a) Octahedron; (b) Cellular gyroid; (c) Sheet gyroid [122]; (d) Zigzag; (e) Palmaz [123]; (f) Negative Poisson's ratio [124] (Copyright 2017, Elsevier; Copyright 2016, Elsevier)

6 Conclusions

(1) Nowadays, in the research about AM-fabricated SMAs, the PBF and DED approaches are preferentially adopted to construct SMAs with higher relative density by appropriately choosing a larger P or a smaller V. Due to the differences in temperature gradient and cooling rate during printing, SMAs possess the distinctive epitaxial solidification phenomenon, which is specifically characterized by the formation of columnar grains and the [001] grain orientation. The desired microstructure can be obtained by controlling the process parameters and processing strategy.

(2) Small changes in alloy composition and scanning parameters can cause a strong response in the phase transformation behavior, including components of solid solution phases and precipitates at equilibrium, and transformation temperature. In particular, the variation of the transformation temperature is significantly dependent on the inhomogeneity of composition, which is induced by the evaporation of elements, elemental burnout, precipitate formation, and mixing of impurity elements.

(3) High-performance SMAs can be built by additive manufacturing. Firstly, the rational selection of scanning parameters, sampling locations and heat treatment processes promotes fine-grain strengthening, precipitation strengthening and dislocation strengthening, which can effectively enhance the strength without excessive loss of fracture strain. Second, the elemental composition, scanning strategy, and heat treatment methods are implemented to influence the combined effects of precipitates, dislocations, twins, and stacking faults, leading to excellent and stable SME and SE. Lastly, modulating alloy composition, governing grain size, and introducing precipitate are expected to prepare elastocaloric cooling materials with large latent heat ΔH, entropy change ΔS, and low hysteresis.

(4) Complex-structure (porous structure) SMAs have been established through AM, which has bright application prospects in aerospace, biomedical and other fields. However, further advancement is required to be realized in materials, technologies, properties, and methods to promote the applicability of AM-prepared SMAs under extreme conditions.

CRediT authorship contribution statement

Yu-xi YANG: Investigation, Writing – Review & editing, Visualization; **Wei-hong GAO:** Supervision,

References

[1]   DEMOLY F, DUNN M L, WOOD K L, QI H J, ANDRÉ J C. The status, barriers, challenges, and future in design for 4D printing [J]. Materials & Design, 2021, 212: 110193.

[2]   XI Xin, LIN Dan-yang, SONG Xiao-guo, LUO Xing-shun, MA Rui, SHI Zhi-feng, BIAN Hong, FU Wei, DONG Zhi-bo, TAN Cai-wang. Strength-plasticity transition mechanism after the solution treatment of GH3230 superalloy fabricated via laser powder bed fusion [J]. Materials Science and Engineering A, 2023, 876: 145124.

[3]   XU Long, JIA Yan-dong, WANG Zhen-hui, WU Shi-wei, JIA Yue-fei, GENG Chuan, PENG Jian-chao, TAN Xiao-hua, WANG Gang. Dual precipitate simultaneous enhancement of tensile and fatigue strength in (FeCoNi)$_{86}$Al$_7$Ti$_7$ high-entropy alloy fabricated using selective laser melting [J]. Journal of Materials Science & Technology, 2023, 148: 90−104.

[4]   LI Bin, SHEN Yi-di, AN Qi. Structural origin of reversible martensitic transformation and reversible twinning in NiTi shape memory alloy [J]. Acta Materialia, 2020, 199: 240−252.

[5]   GAO Wei-hong, YI Xiao-yang, SUN Bin, MENG Xiang-long, CAI Wei, ZHAO Lian-cheng. Microstructural evolution of martensite during deformation in Zr$_{50}$Cu$_{50}$ shape memory alloy [J]. Acta Materialia, 2017, 132: 405−415.

[6]   XI Rui, JIANG Hao, KUSTOV S, ZHANG Zhi-hui, ZHAO Guo-qun, VANMEENSEL K, van HUMBEECK J, WANG Xie-bin. Influence of Nb addition and process parameters on the microstructure and phase transformation behavior of NiTiNb ternary shape memory alloys fabricated by laser powder bed fusion [J]. Scripta Materialia, 2023, 222: 114996.

[7]   TIAN Yin-bao, CHEN Xin-ya, CAI Yang-chuan, LUO Zhen, CHEN Min-fang, ZHANG Xi, LI Jian-guo, HAN Jian. Microstructure and properties of a Ni−Ti−Cr−Mo−Nb alloy fabricated in situ by dual-wire arc additive manufacturing [J]. Materials Science and Engineering A, 2022, 853: 143740.

[8]   ZUO Xin-da, ZHANG Wei, CHEN Yi, OLIVEIRA J P, ZENG Zhi, LI Yang, LUO Zhen, AO S. Wire-based directed energy deposition of NiTiTa shape memory alloys: Microstructure, phase transformation, electrochemistry, X-ray visibility and mechanical properties [J]. Additive Manufacturing, 2022, 59: 103115.

[9]   BABACAN N, PAULY S, GUSTMANN T. Laser powder bed fusion of a superelastic Cu−Al−Mn shape memory alloy [J]. Materials & Design, 2021, 203: 109625.

[10]   FERRETTO I, BORZì A, KIM D, VENTURA N M D, HOSSEINI E, LEE W J, LEINENBACH C. Control of microstructure and shape memory properties of a Fe−Mn−Si-based shape memory alloy during laser powder bed fusion [J]. Additive Manufacturing Letters, 2022, 3: 100091.

[11]   LAITINEN V, SAREN A, SOZINOV A, ULLAKKO K. Giant 5.8% magnetic-field-induced strain in additive manufactured Ni−Mn−Ga magnetic shape memory alloy [J]. Scripta Materialia, 2022, 208: 114324.

[12]   SUN Wen, LU Xiang, WEI Zhi-yang, LI Qiang, LI Zong-bin, ZHANG Yi-fei, LIU Jian. Multicaloric effect in Ni–Mn–Sn metamagnetic shape memory alloys by laser powder bed fusion [J]. Additive Manufacturing, 2022, 59: 103125.

[13]   JIA Wu-ming, CHEN Sui-yuan, WANG Lu-ting, SHANG Fan-min, SUN Xin-ru, YANG Dong-rui. Microstructure and properties of Ni−Co−Mn−Al magnetic shape memory alloy prepared by direct laser deposition and heat treatment [J]. Optics & Laser Technology, 2021, 141: 107119.

[14]   LAUHOFF C, SOMMER N, VOLLMER M, MIENERT G, KROOß P, BÖHM S, NIENDORF T. Excellent superelasticity in a Co−Ni−Ga high-temperature shape memory alloy processed by directed energy deposition [J]. Materials Research Letters, 2020, 8(8): 314−320.

[15]   MUNTASIR BILLAH A H M, RAHMAN J, ZHANG Q. Shape memory alloys (SMAs) for resilient bridges: A state-of-the-art review [J]. Structures, 2022, 37: 514−527.

[16]   KIM H I, HAN M W, SONG S H, AHN S H. Soft morphing hand driven by SMA tendon wire [J]. Composites Part B: Engineering, 2016, 105: 138−148.

[17]   SILVA G C, SILVESTRE F J, DONADON M V. A nonlinear aerothermoelastic model for slender composite beam-like wings with embedded shape memory alloys [J]. Composite Structures, 2022, 287: 115367.

[18]   HERZOG D, SEYDA V, WYCISK E M, EMMELMANN C. Additive Manufacturing of Metals [J]. Acta Materialia, 2016, 117: 371−392.

[19]   PARVIZI S, HASHEMI S M, ASGARINIA F, NEMATOLLAHI M, ELAHINIA M. Effective parameters on the final properties of NiTi-based alloys manufactured by powder metallurgy methods: A review [J]. Progress in Materials Science, 2021, 117: 100739.

[20]   ALAGHA A N, HUSSAIN S, ZAKI W. Additive manufacturing of shape memory alloys: A review with emphasis on powder bed systems [J]. Materials & Design, 2021, 204: 109654.

[21] SAMES W J, LIST F A, PANNALA S, DEHOFF R R, BABU S S. The metallurgy and processing science of metal additive manufacturing [J]. International Materials Reviews, 2016, 61(5): 315−360.

[22] MOSTAFAEI A, RODRIGUEZ DE VECCHIS P, STEVENS E L, CHMIELUS M. Sintering regimes and resulting microstructure and properties of binder jet 3D printed Ni−Mn−Ga magnetic shape memory alloys [J]. Acta Materialia, 2018, 154: 355−364.

[23] LU H Z, MA H W, YANG Y, CAI W S, LUO X, YAN A, KANG L M, YIN S, YANG C. Tailoring phase transformation behavior, microstructure, and superelasticity of NiTi shape memory alloys by specific change of laser power in selective laser melting [J]. Materials Science and Engineering A, 2023, 864: 144576.

[24] SING S L, YEONG W Y. Laser powder bed fusion for metal additive manufacturing: perspectives on recent developments [J]. Virtual and Physical Prototyping, 2020, 15(3): 359−370.

[25] CALIGNANO F, MANFREDI D, AMBROSIO E P, BIAMINO S, LOMBARDI M, ATZENI E, SALMI A, MINETOLA P, IULIANO L, FINO P. Overview on additive manufacturing technologies [J]. Proceedings of the IEEE, 2017, 105(4): 593−612.

[26] LI Yang-ping, WANG Chang-rui, DU Xiao-dong, TIAN Wei, ZHANG Tao, HU Jun-shan, LI Bo, LI Peng-cheng, LIAO Wen-he. Research status and quality improvement of wire arc additive manufacturing of metals [J]. Transactions of Nonferrous Metals Society of China, 2023, 33(4): 969−996.

[27] SVETLIZKY D, DAS M, ZHENG B, VYATSKIKH A L, BOSE S, BANDYOPADHYAY A, SCHOENUNG J M, LAVERNIA E J, ELIAZ N. Directed energy deposition (DED) additive manufacturing: Physical characteristics, defects, challenges and applications [J]. Materials Today, 2021, 49: 271−295.

[28] WILLIAMS S W, MARTINA F, ADDISON A C, DING J, PARDAL G, COLEGROVE P. Wire + arc additive manufacturing [J]. Materials Science and Technology, 2016, 32(7): 641−647.

[29] HOOPER P A. Melt pool temperature and cooling rates in laser powder bed fusion [J]. Additive Manufacturing, 2018, 22: 548−559.

[30] AL-BERMANI S S, BLACKMORE M L, ZHANG W, TODD I. The origin of microstructural diversity, texture, and mechanical properties in electron beam melted Ti−6Al−4V [J]. Metallurgical and Materials Transactions A, 2010, 41: 3422−3434.

[31] SHAMSAEI N, YADOLLAHI A, BIAN L, THOMPSON S M. An overview of direct laser deposition for additive manufacturing. Part II: Mechanical behavior, process parameter optimization and control [J]. Additive Manufacturing, 2015, 8: 12−35.

[32] KOK Y, TAN X P, WANG P, NAI M L S, LOH N H, LIU E, TOR S B. Anisotropy and heterogeneity of microstructure and mechanical properties in metal additive manufacturing: A critical review [J]. Materials & Design, 2018, 139: 565−586.

[33] WANG C, TAN X P, DU Z, CHANDRA S, SUN Z, LIM C W J, TOR S B, LIM C S, WONG C H. Additive manufacturing of NiTi shape memory alloys using pre-mixed powders [J]. Journal of Materials Processing Technology, 2019, 271: 152−161.

[34] PU Z, DU D, WANG K, LIU G, ZHANG D, WANG X, CHANG B. Microstructure, phase transformation behavior and tensile superelasticity of NiTi shape memory alloys fabricated by the wire-based vacuum additive manufacturing [J]. Materials Science and Engineering A, 2021, 812: 141077.

[35] PU Ze, DU Dong, WANG Kai-ming, LIU Guan, ZHANG Dong-qi, WANG Xie-bin, CHANG Bao-hua. Influence of laser power on microstructure and tensile property of a new nickel-based superalloy designed for additive manufacturing [J]. Transactions of Nonferrous Metals Society of China, 2023, 33(4): 1124−1143.

[36] YAO Xin-Xin, LI Jian-Yu, WANG Yi-fei, GAO Xiang, ZHANG Zhao. Numerical simulation of powder effect on solidification in directed energy deposition additive manufacturing [J]. Transactions of Nonferrous Metals Society of China, 2021, 31(9): 2871−2884.

[37] YUE Tian-Yang, ZHANG Sheng, WANG Chao-Yue, XU Wei, XU Yi-Di, SHI Yu-Sheng, ZANG Yong. Effects of selective laser melting parameters on surface quality and densification behaviours of pure nickel [J]. Transactions of Nonferrous Metals Society of China, 2022, 32(8): 2634−2647.

[38] SAFDEL A, ELBESTAWI M A. New insights on the laser powder bed fusion processing of a NiTi alloy and the role of dynamic restoration mechanisms [J]. Journal of Alloys and Compounds, 2021, 885: 160971.

[39] LU H Z, MA H W, CAI W S, LUO X, QU S G, WANG J, LUPOI R, YIN S, YANG C. Altered phase transformation behaviors and enhanced bending shape memory property of NiTi shape memory alloy via selective laser melting [J]. Journal of Materials Processing Technology, 2022, 303: 117546.

[40] GAN Jie, DUAN Long-chen, LI Fei, CHE Yu-si, ZHOU Yan, WEN Shi-feng, YAN Chun-ze. Effect of laser energy density on the evolution of Ni_4Ti_3 precipitate and property of NiTi shape memory alloys prepared by selective laser melting [J]. Journal of Alloys and Compounds, 2021, 869: 159338.

[41] LU H Z, YANG C, LUO X, MA H W, SONG B, LI Y Y, ZHANG L C. Ultrahigh-performance TiNi shape memory alloy by 4D printing [J]. Materials Science and Engineering A, 2019, 763: 138166.

[42] YU Zheng-lei, XU Ze-zhou, GUO Yun-ting, XIN Ren-long, LIU Rui-yao, JIANG Chao-rui, LI Lun-xiang, ZHANG Zhi-hui, REN Lu-quan. Study on properties of SLM-NiTi shape memory alloy under the same energy density [J]. Journal of Materials Research and Technology, 2021, 13: 241−250.

[43] LU H Z, MA H W, CAI W S, LUO X, WANG Z, SONG C H, YIN S, YANG C. Stable tensile recovery strain induced by a Ni_4Ti_3 nanoprecipitate in a $Ni_{50.4}Ti_{49.6}$ shape memory alloy fabricated via selective laser melting [J]. Acta Materialia, 2021, 219: 117261.

[44] REN D C, ZHANG H B, LIU Y J, LI S J, JIN W, YANG R, ZHANG L C. Microstructure and properties of equiatomic Ti−Ni alloy fabricated by selective laser melting [J]. Materials Science and Engineering A, 2020, 771: 138586.

[45] CAO Yu-xian, ZHOU Xiang-lin, CONG Dao-yong, ZHENG Hong-xing, CAO Yi-huan, NIE Zhi-hua, CHEN Zhen, LI Shao-hui, XU Ning, GAO Zhi-yong, CAI Wei, WANG Yan-dong. Large tunable elastocaloric effect in additively manufactured Ni−Ti shape memory alloys [J]. Acta Materialia, 2020, 194: 178−189.

[46] SAEDI S, TURABI A S, ANDANI M T, MOGHADDAM N S, ELAHINIA M, KARACA H E. Texture, aging, and superelasticity of selective laser melting fabricated Ni-rich NiTi alloys [J]. Materials Science and Engineering A, 2017, 686: 1−10.

[47] ZHAO Chun-yang, LIANG Hai-long, LUO Shun-cun, YANG Jing-jing, WANG Ze-min. The effect of energy input on reaction, phase transition and shape memory effect of NiTi alloy by selective laser melting [J]. Journal of Alloys and Compounds, 2020, 817: 153288.

[48] WANG Xie-bin, YU Jing-ya, LIU Jiang-wei, CHEN Liu-gang, YANG Qin, WEI Hui-liang, SUN Jie, WANG Zuo-cheng, ZHANG Zhi-hui, ZHAO Guo-qun, van HUMBEECK J. Effect of process parameters on the phase transformation behavior and tensile properties of NiTi shape memory alloys fabricated by selective laser melting [J]. Additive Manufacturing, 2020, 36: 101545.

[49] CHEN Gang, LIU Shu-ying, HUANG Chao, MA Yuan, LI Ying, ZHANG Bai-cheng, GAO Lei, ZHANG Bo-wei, WANG Pei, QU Xuan-hui. In-situ phase transformation and corrosion behavior of TiNi via LPBF [J]. Corrosion Science, 2022, 203: 110348.

[50] LU H Z, LIU L H, YANG C, LUO X, SONG C H, WANG Z, WANG J, SU Y D, DING Y F, ZHANG L C, LI Y Y. Simultaneous enhancement of mechanical and shape memory properties by heat-treatment homogenization of Ti_2Ni precipitates in TiNi shape memory alloy fabricated by selective laser melting [J]. Journal of Materials Science & Technology, 2022, 101: 205−216.

[51] XIONG Zhi-wei, LI Zhong-han, SUN Zhen, HAO Shi-jie, YANG Ying, LI Meng, SONG Chang-hui, QIU Ping, CUI Li-shan. Selective laser melting of NiTi alloy with superior tensile property and shape memory effect [J]. Journal of Materials Science & Technology, 2019, 35: 2238−2242.

[52] MA Cheng-long, WU Mei-ping, DAI Dong-hua, XIA Mu-jian. Stress-induced heterogeneous transformation and recoverable behavior of laser powder bed fused Ni-rich $Ni_{50.6}Ti_{49.4}$ alloys without post treatment [J]. Journal of Alloys and Compounds, 2022, 905: 164212.

[53] CHEN Wen-liang, YANG Qin, HUANG Shu-ke, HUANG Shi-yang, KRUZIC J J, LI Xiao-ping. Laser power modulated microstructure evolution, phase transformation and mechanical properties in NiTi fabricated by laser powder bed fusion [J]. Journal of Alloys and Compounds, 2021, 861: 157959.

[54] NEMATOLLAHI M, SAGHAIAN S E, SAFAEI K, BAYATI P, BASSANI P, BIFFI C, TUISSI A, KARACA H, ELAHINIA M. Building orientation−structure−property in laser powder bed fusion of NiTi shape memory alloy [J]. Journal of Alloys and Compounds, 2021, 873: 159791.

[55] CHEKOTU J C, GOODALL R, KINAHAN D, BRABAZON D. Control of Ni−Ti phase structure, solid-state transformation temperatures and enthalpies via control

of L-PBF process parameters [J]. Materials & Design, 2022, 218: 110715.

[56] WEN Shi-feng, LIU Yang, ZHOU Yan, ZHAO Ai-guo, YAN Chun-ze, SHI Yu-sheng. Effect of Ni content on the transformation behavior and mechanical property of NiTi shape memory alloys fabricated by laser powder bed fusion [J]. Optics & Laser Technology, 2021, 134: 106653.

[57] GU Dong-dong, MA Cheng-long, DAI Dong-hua, YANG Jian-kai, LIN Kai-jie, ZHANG Hong-mei, ZHANG Han. Additively manufacturing-enabled hierarchical NiTi-based shape memory alloys with high strength and toughness [J]. Virtual and Physical Prototyping, 2021, 16(Suppl.): 19−38.

[58] LU H Z, CHEN T, LIU L H, WANG H, LUO X, SONG C H, WANG Z, YANG C. Constructing function domains in NiTi shape memory alloys by additive manufacturing [J]. Virtual and Physical Prototyping, 2022, 17(3): 563−581.

[59] FENG Yan, LIU Bo-chao, WAN Xue-man, LIU Qian-wen, LIN Xin, WANG Pan. Influence of processing parameter on phase transformation and superelastic recovery strain of laser solid forming NiTi alloy [J]. Journal of Alloys and Compounds, 2022, 908: 164568.

[60] WAN Xue-man, FENG Yan, LIN Xin, TAN Hua. Large superelastic recovery and elastocaloric effect in as-deposited additive manufactured $Ni_{50.8}Ti_{49.2}$ alloy [J]. Applied Physics Letters, 2019, 114: 221903.

[61] NEMATOLLAHI M, TOKER G P, SAFAEI K, HINOJOS A, SAGHAIAN S E, BENAFAN O, MILLS M J, KARACA H, ELAHINIA M. Laser powder bed fusion of NiTiHf high-temperature shape memory alloy: Effect of process parameters on the thermomechanical behavior [J]. Metals, 2020, 10: 1522.

[62] XU Ze-zhou, GUO Yun-ting, LIU Yu-ting, YU Zheng-lei, ZHANG Zhi-hui, REN Lu-quan. The martensitic transformation behavior and shape memory effect of laser powder bed fusion NiTi alloys influenced by rare earth addition [J]. Materials Science and Engineering A, 2022, 848: 143350.

[63] XI Xiao-ying, ZHANG Jian-tao, TANG Hao, CAO Yang, XIAO Zhi-yu. The ultrahigh functional response of CuAlMnNb shape memory alloy by selective laser melting [J]. Journal of Materials Research and Technology, 2022, 20: 671−680.

[64] ZHUO Lin-rong, SONG Bo, LI Rui-di, WEI Qing-dong, YAN Chun-ze, SHI Yu-sheng. Effect of element evaporation on the microstructure and properties of CuZnAl shape memory alloys prepared by selective laser melting [J]. Optics & Laser Technology, 2020, 127: 106164.

[65] GUSTMANN T, NEVES A, KÜHN U, GARGARELLA P, KIMINAMI C S, BOLFARINI C, ECKERT J, PAULY S. Influence of processing parameters on the fabrication of a Cu−Al−Ni−Mn shape-memory alloy by selective laser melting [J]. Additive Manufacturing, 2016, 11: 23−31.

[66] TIAN Jian, ZHU Wen-zhi, WEI Qing-song, WEN Shi-feng, LI Shuai, SONG Bo, SHI Yu-sheng. Process optimization, microstructures and mechanical properties of a Cu-based shape memory alloy fabricated by selective laser melting [J]. Journal of Alloys and Compounds, 2019, 785: 754−764.

[67] GUSTMANN T, DOS SANTOS J M, GARGARELLA P, KÜHN U, VAN HUMBEECK J, PAULY S. Properties of

Cu-based shape-memory alloys prepared by selective laser melting [J]. Shape Memory and Superelasticity, 2017, 3(1): 24−36.

[68] KIM D, FERRETTO I, KIM W, LEINENBACH C, LEE W. Effect of post-heat treatment conditions on shape memory property in 4D printed Fe−17Mn−5Si−10Cr−4Ni shape memory alloy [J]. Materials Science and Engineering A, 2022, 852: 143689.

[69] KIM D, FERRETTO I, JEON J B, LEINENBACH C, LEE W. Formation of metastable bcc-δ phase and its transformation to fcc-γ in laser powder bed fusion of Fe−Mn−Si shape memory alloy [J]. Journal of Materials Research and Technology, 2021, 14: 2782−2788.

[70] FERRETTO I, KIM D, DELLA VENTURA N M, SHAHVERDI M, LEE W, LEINENBACH C. Laser powder bed fusion of a Fe−Mn−Si shape memory alloy [J]. Additive Manufacturing, 2021, 46: 102071.

[71] ZHANG Dong-zhe, LI Yun-ze, CONG Wei-long. Multi-scale pseudoelasticity of NiTi alloys fabricated by laser additive manufacturing [J]. Materials Science and Engineering A, 2021, 821: 141600.

[72] GAO S, WENG F, BODUNDE O P, QIN M, LIAO W H, GUO P. Spatial characteristics of nickel-titanium shape memory alloy fabricated by continuous directed energy deposition [J]. Journal of Manufacturing Processes, 2021, 71: 417−428.

[73] GAO Shi-ming, BODUNDE O P, QIN Mian, LIAO W H, GUO Ping. Microstructure and phase transformation of nickel-titanium shape memory alloy fabricated by directed energy deposition with in-situ heat treatment [J]. Journal of Alloys and Compounds, 2022, 898: 162896.

[74] BARAN A, POLANSKI M. Microstructure and properties of LENS (laser engineered net shaping) manufactured Ni−Ti shape memory alloy [J]. Journal of Alloys and Compounds, 2018, 750: 863−870.

[75] BIMBER B A, HAMILTON R F, KEIST J, PALMER T A. Anisotropic microstructure and superelasticity of additive manufactured NiTi alloy bulk builds using laser directed energy deposition [J]. Materials Science and Engineering A, 2016, 674: 125−134.

[76] LI Bing-qiang, WANG Liang, WANG Bin-bin, LI Dong-hai, CUI Ran, SU Bao-xian, YAO Long-hui, LUO Liang-shun, CHEN Rui-run, SU Yan-qing, GUO Jing-jie, FU Heng-zhi. Solidification characterization and its correlation with the mechanical properties and functional response of NiTi shape memory alloy manufactured by electron beam freeform fabrication [J]. Additive Manufacturing, 2021, 48: 102468.

[77] LI Bing-qiang, WANG Liang, WANG Bin-bin, LI Dong-hai, OLIVEIRA J P, CUI Ran, YU Jian-xin, LUO Liang-shun, CHEN Rui-run, SU Yan-qing, GUO Jing-jie, FU Heng-zhi. Tuning the microstructure, martensitic transformation and superelastic properties of EBF³-fabricated NiTi shape memory alloy using interlayer remelting [J]. Materials & Design, 2022, 220: 110886.

[78] LI Bing-qiang, WANG Liang, WANG Bin-bin, LI Dong-hai, OLIVEIRA J P, CUI Ran, YU Jian-xin, LUO Liang-shun, CHEN Rui-run, SU Yan-qing, GUO Jing-jie, FU Heng-zhi. Electron beam freeform fabrication of NiTi shape memory alloys: Crystallography, martensitic transformation, and

functional response [J]. Materials Science and Engineering A, 2022, 843: 143135.

[79] HAN Jian, CHEN Xin-ya, ZHANG Guo-yang, LU Lian-zhong, XIN Yi, LIU Bang, CAI Yang-chuan, ZHANG Xi, TIAN Yin-bao. Microstructure and mechanical properties of Ni$_{50.8}$Ti$_{49.2}$ and Ni$_{53}$Ti$_{47}$ alloys prepared in situ by wire-arc additive manufacturing [J]. Journal of Materials Processing Technology, 2022, 306: 117631.

[80] LIU Gao-feng, ZHOU Shi-hui, LIN Peng-yu, ZONG Xue-mei, CHEN Zhi-kai, ZHANG Zhi-hui, REN Lu-quan. Analysis of microstructure, mechanical properties, and wear performance of NiTi alloy fabricated by cold metal transfer based wire arc additive manufacturing [J]. Journal of Materials Research and Technology, 2022, 20: 246−259.

[81] WANG Jun, PAN Zeng-xi, CARPENTER K, HAN Jian, WANG Zhi-yang, LI Hui-jun. Comparative study on crystallographic orientation, precipitation, phase transformation and mechanical response of Ni-rich NiTi alloy fabricated by WAAM at elevated substrate heating temperatures [J]. Materials Science and Engineering A, 2021, 800: 140307.

[82] ZENG Z, CONG B Q, OLIVEIRA J P, KE W C, SCHELL N, PENG B, QI Z W, GE F G, ZHANG W, AO S S. Wire and arc additive manufacturing of a Ni-rich NiTi shape memory alloy: Microstructure and mechanical properties [J]. Additive Manufacturing, 2020, 32: 101051.

[83] RESNINA N, PALANI I A, BELYAEV S, PRABU S S M, LIULCHAK P, KARASEVA U, MANIKANDAN M, JAYACHANDRAN S, BRYUKHANOVA V, SAHU A, BIKBAEV R. Structure, martensitic transformations and mechanical behaviour of NiTi shape memory alloy produced by wire arc additive manufacturing [J]. Journal of Alloys and Compounds, 2021, 851: 156851.

[84] YU Lin, CHEN Ke-yu, ZHANG Yuan-ling, LIU Jie, YANG Lei, SHI Yu-sheng. Microstructures and mechanical properties of NiTi shape memory alloys fabricated by wire arc additive manufacturing [J]. Journal of Alloys and Compounds, 2022, 892: 162193.

[85] SHIVA S, PALANI I A, PAUL C P, MISHRA S K, SINGH B. Investigations on phase transformation and mechanical characteristics of laser additive manufactured TiNiCu shape memory alloy structures [J]. Journal of Materials Processing Technology, 2016, 238: 142−151.

[86] SHIVA S, YADAIAH N, PALANI I A, PAUL C P, BINDRA K S. Thermo mechanical analyses and characterizations of TiNiCu shape memory alloy structures developed by laser additive manufacturing [J]. Journal of Manufacturing Processes, 2019, 48: 98−109.

[87] LU Bing-wen, CUI Xiu-fang, MA Wen-you, DONG Mei-ling, FANG Yong-chao, WEN Xin, JIN Guo, ZENG De-chang. Promoting the heterogeneous nucleation and the functional properties of directed energy deposited NiTi alloy by addition of La$_2$O$_3$ [J]. Additive Manufacturing, 2020, 33: 101150.

[88] HABERLAND C, ELAHINIA M, WALKER J M, MEIER H, FRENZEL J. On the development of high quality NiTi shape memory and pseudoelastic parts by additive manufacturing [J]. Smart Materials and Structures, 2014, 23(10): 104002.

[89] NIEDBALSKI S, DURáN A, WALCZAK M, RAMOS-

GREZ J A. Laser-assisted synthesis of Cu−Al−Ni shape memory alloys: Effect of inert gas pressure and Ni content [J]. Materials (Basel), 2019, 12(5): 12050794.

[90] XUE L, ATLI K C, PICAK S, ZHANG C, ZHANG B, ELWANY A, ARROYAVE R, KARAMAN I. Controlling martensitic transformation characteristics in defect-free NiTi shape memory alloys fabricated using laser powder bed fusion and a process optimization framework [J]. Acta Materialia, 2021, 215: 117017.

[91] ZHANG Chen, XUE Lei, PESTKA S A, RANAIEFAR M, ATLI K C, HONARMANDI P, ARRÓYAVE R, KARAMAN I, ELWANY A. Processing parameters and martensitic phase transformation relationships in near defect-free additively manufactured NiTiHf high temperature shape memory alloys [J]. Materials & Design, 2022, 222: 110988.

[92] FARHANG B, RAVICHANDER B B, VENTURI F, AMERINATANZI A, SHAYESTEH MOGHADDAM N. Study on variations of microstructure and metallurgical properties in various heat-affected zones of SLM fabricated nickel–titanium alloy [J]. Materials Science and Engineering A, 2020, 774: 138919.

[93] SCIPIONI BERTOLI U, WOLFER A J, MATTHEWS M J, DELPLANQUE J P R, SCHOENUNG J M. On the limitations of volumetric energy density as a design parameter for selective laser melting [J]. Materials & Design, 2017, 113: 331−340.

[94] BIFFI C A, TUISSI A, DEMIR A G. Martensitic transformation, microstructure and functional behavior of thin-walled Nitinol produced by micro laser metal wire deposition [J]. Journal of Materials Research and Technology, 2021, 12: 2205−2215.

[95] GUSTMANN T, SCHWAB H, KüHN U, PAULY S. Selective laser remelting of an additively manufactured Cu−Al−Ni−Mn shape-memory alloy [J]. Materials & Design, 2018, 153: 129−138.

[96] ABOLHASANI D, HAN S W, VANTYNE C J, KANG N, MOON Y H. Powder bed fusion of two-functional Cu−Al−Ni shape memory alloys utilized for 4D printing [J]. Journal of Alloys and Compounds, 2022, 922: 166228.

[97] FU Jin, HU Zhi-heng, SONG Xu, ZHAI Wei, LONG Yu, LI Heng, FU Ming-wang. Micro selective laser melting of NiTi shape memory alloy: Defects, microstructures and thermal/mechanical properties [J]. Optics & Laser Technology, 2020, 131: 106374.

[98] EHSAN SAGHAIAN S, NEMATOLLAHI M, TOKER G, HINOJOS A, SHAYESTEH MOGHADDAM N, SAEDI S, LU C Y, JAVAD MAHTABI M, MILLS M J, ELAHINIA M, KARACA H E. Effect of hatch spacing and laser power on microstructure, texture, and thermomechanical properties of laser powder bed fusion (L-PBF) additively manufactured NiTi [J]. Optics & Laser Technology, 2022, 149: 107680.

[99] REN Qian-hong, CHEN Chao-yue, LU Zhan-jun, WANG Xie-bin, LU Hai-zhou, YIN Shuo, LIU Yi, LI Hua, WANG Jiang, REN Zhong-ming. Effect of a constant laser energy density on the evolution of microstructure and mechanical properties of NiTi shape memory alloy fabricated by laser powder bed fusion [J]. Optics & Laser Technology, 2022, 152: 108182.

[100] PU Ze, DU Dong, WANG Kai-ming, LIU Guan, ZHANG Dong-qi, ZHANG Hao-yu, XI Rui, WANG Xie-bin, CHANG Bao-hua. Study on the NiTi shape memory alloys in-situ synthesized by dual-wire-feed electron beam additive manufacturing [J]. Additive Manufacturing, 2022, 56: 102886.

[101] ZHANG Mu-gong, FANG Xue-wei, WANG Yang, JIANG Xiao, CHANG Tian-xing, XI Nai-yuan, HUANG Ke. High superelasticity NiTi fabricated by cold metal transfer based wire arc additive manufacturing [J]. Materials Science and Engineering A, 2022, 840: 143001.

[102] MA Cheng-long, GU Dong-dong, SETCHI R, DAI Dong-hua, WU Mei-ping, MA Shuai, MIAO Xiao-jin. A large compressive recoverable strain induced by heterogeneous microstructure in a $Ni_{50.6}Ti_{49.4}$ shape memory alloy via laser powder bed fusion and subsequent aging treatment [J]. Journal of Alloys and Compounds, 2022, 918: 165620.

[103] NAGARAJAN R, CHATTOPADHYAY K. Intermetallic $Ti_2Ni/TiNi$ nanocomposite by rapid solidification [J]. Acta Metallurgica et Materialia, 1994, 42: 947−958.

[104] NAJI H, KHALIL-ALLAFI J, KHALILI V. Microstructural characterization and quantitative phase analysis of Ni-rich NiTi after stress assisted aging for long times using the Rietveld method [J]. Materials Chemistry and Physics, 2020, 241: 122317.

[105] LIU Shan, LIN Yao, WANG Guang-chun, WANG Xie-bin. Effect of varisized Ni_4Ti_3 precipitate on the phase transformation behavior and functional stability of Ti−50.8at.%Ni alloys [J]. Materials Characterization, 2021, 172: 110832.

[106] FERRETTO I, KIM D, MOHRI M, GHAFOORI E, LEE W J, LEINENBACH C. Shape recovery performance of a (V,C)-containing Fe−Mn−Si−Ni−Cr shape memory alloy fabricated by laser powder bed fusion [J]. Journal of Materials Research and Technology, 2022, 20: 3969−3984.

[107] ZHANG Qing-quan, HAO Shi-jie, LIU Yu-ting, XIONG Zhi-wei, GUO Wen-qian, YANG Ying, REN Yang, CUI Li-shan, REN L, ZHANG Z. The microstructure of a selective laser melting (SLM)-fabricated NiTi shape memory alloy with superior tensile property and shape memory recoverability [J]. Applied Materials Today, 2020, 19: 100547.

[108] CHEN Yu-hong, REN Shu-bin, ZHAO Yang, QU Xuan-hui. Microstructure and properties of CuCr alloy manufactured by selective laser melting [J]. Journal of Alloys and Compounds, 2019, 786: 189−197.

[109] ELAHINIA M, SHAYESTEH MOGHADDAM N, AMERINATANZI A, SAEDI S, TOKER G P, KARACA H, BIGELOW G S, BENAFAN O. Additive manufacturing of NiTiHf high temperature shape memory alloy [J]. Scripta Materialia, 2018, 145: 90−94.

[110] SAM J, FRANCO B, MA J, KARAMAN I, ELWANY A, MABE J H. Tensile actuation response of additively manufactured nickel-titanium shape memory alloys [J]. Scripta Materialia, 2018, 146: 164−168.

[111] DASGUPTA R. A look into Cu-based shape memory alloys: Present scenario and future prospects [J]. Journal of Materials Research, 2014, 29(16): 1681−1698.

[112] FENG Bo, WANG Cheng, ZHANG Qing-quan, REN Yang, CUI Li-shan, YANG Qin, HAO Shi-jie. Effect of laser hatch

spacing on the pore defects, phase transformation and properties of selective laser melting fabricated NiTi shape memory alloys [J]. Materials Science and Engineering A, 2022, 840: 142965.

[113] CHOWDHURY P, PATRIARCA L, REN G, SEHITOGLU H. Molecular dynamics modeling of NiTi superelasticity in presence of nanoprecipitates [J]. International Journal of Plasticity, 2016, 81: 152−167.

[114] XIONG Zhi-wei, LI Hao-hang, YANG Hong, YANG Ying, LIU Yi-nong, CUI Li-shan, LI Xiao-xiao, MASSELING L, SHEN Li-yaowei, HAO Shi-jie. Micro laser powder bed fusion of NiTi alloys with superior mechanical property and shape recovery function [J]. Additive Manufacturing, 2022, 57: 102960.

[115] POLATIDIS E, ŠMíD M, KUBĚNA I, HSU W N, LAPLANCHE G, VAN SWYGENHOVEN H. Deformation mechanisms in a superelastic NiTi alloy: An in-situ high resolution digital image correlation study [J]. Materials & Design, 2020, 191: 108622.

[116] PU Ze, DU Dong, WANG Kai-ming, LIU Guan, ZHANG Dong-qi, LIANG Zhi-yue, XI Rui, WANG Xie-bin, CHANG Bao-hua. Evolution of transformation behavior and tensile functional properties with process parameters for electron beam wire-feed additive manufactured NiTi shape memory alloys [J]. Materials Science and Engineering A, 2022, 840: 142977.

[117] HOU Hui-long, SIMSEK E, STASAK D, HASAN N A, QIAN Su-xin, OTT R, CUI Jun, TAKEUCHI I. Elastocaloric cooling of additive manufactured shape memory alloys with large latent heat [J]. Journal of Physics D: Applied Physics, 2017, 50: 404001.

[118] HOU Hui-long, SIMSEK E, MA T, JOHNSON N S, QIAN Su-xin, CISSé C, STASAK D, AL HASAN N, ZHOU Lin, HWANG Y, RADERMACHER R, LEVITAS V I, KRAMER M J, ZAEEM M A, STEBNER A P, OTT R T, CUI J, TAKEUCHI I. Fatigue-resistant high-performance elastocaloric materials made by additive manufacturing [J]. Science, 2019, 366(6469): 1116−1121.

[119] MCCUE I D, VALENTINO G M, TRIGG D B, LENNON A M, HEBERT C E, SEKER D P, NIMER S M, MASTANDREA J P, TREXLER M M, STORCK S M. Controlled shape-morphing metallic components for deployable structures [J]. Materials & Design, 2021, 208: 109935.

[120] XU Yue-sheng, QIU Lei, YUAN Shen-fang, WANG Yu. Research on shape memory alloy honeycomb structures fabricated by selective laser melting additive manufacturing [J]. Optics & Laser Technology, 2022, 152: 108160.

[121] ZHAO Meng, QING Huai-bin, WANG Yong-xin, LIANG Jin, ZHAO Meng-yao, GENG Yong-liang, LIANG Jun-zhe, LU Bing-heng. Superelastic behaviors of additively manufactured porous NiTi shape memory alloys designed with Menger sponge-like fractal structures [J]. Materials & Design, 2021, 200: 109448.

[122] SPEIRS M, VAN HOOREWEDER B, VAN HUMBEECK J, KRUTH J P. Fatigue behaviour of NiTi shape memory alloy scaffolds produced by SLM, a unit cell design comparison [J]. Journal of the Mechanical Behavior of Biomedical Materials, 2017, 70: 53−59.

[123] JAMSHIDI P, PANWISAWAS C, LANGI E, COX S C, FENG J, ZHAO L, ATTALLAH M M. Development, characterisation, and modelling of processability of nitinol stents using laser powder bed fusion [J]. Journal of Alloys and Compounds, 2022, 909: 164681.

[124] LI Sheng, HASSANIN H, ATTALLAH M M, ADKINS N J E, ESSA K. The development of TiNi-based negative Poisson's ratio structure using selective laser melting [J]. Acta Materialia, 2016, 105: 75−83.

增材制造形状记忆合金的最新进展

杨雨茜 [1]，高卫红 [1]，孙 斌 [1]，傅宇东 [1]，孟祥龙 [2]

1. 哈尔滨工程大学 材料科学与化学工程学院，哈尔滨 150001；
2. 哈尔滨工业大学 材料科学与工程学院，哈尔滨 150001

摘 要：增材制造(AM)作为一项革命性技术，能够以前所未有的自由度制造复杂的形状记忆合金(SMA)部件，从而为现代制造业的发展以及传统制造业的转型提供巨大契机。本篇综述从微观结构、性能和前景的角度阐明增材制造形状记忆合金的研究进展，为制备具有高性能和多功能性的理想材料拓宽思路。改变扫描参数能够有效调控打印过程中独特的微观组织——外延凝固形成的柱状晶粒。在析出相、位错、孪晶与层错等微观结构的综合影响下可获得优异且稳定的形状记忆效应与超弹性。最后，仍需要在材料、技术、性能和方法等方面取得进一步突破，以促进增材制造形状记忆合金在各行业中的应用。

关键词：形状记忆合金；增材制造；外延凝固；马氏体转变；工艺参数控制

(Edited by Bing YANG)